# Sufficient conditions for the existence of *Q* balls in gauge theories

A. Kusenko[a] and M. Shaposhnikov[b]
*Theory Division, CERN, CH-1211 Geneva 23, Switzerland*

P. G. Tinyakov[c]
*Institute for Nuclear Research, 117312 Moscow, Russia*

(Submitted 9 January 1998)
Pis'ma Zh. Éksp. Teor. Fiz. **67**, No. 4, 229–232 (25 February 1998)

A set of simple sufficient conditions for the existence of *Q* balls in gauge theories is formulated. © *1998 American Institute of Physics.* [S0021-3640(98)00104-2]

PACS numbers: 11.15.−q, 11.30.Pb

Abelian *Q* balls are nontopological solitons that accommodate some conserved global charge at a lower energy cost than would a collection of free scalar particles.[1,2] They exist in theories that preserve some global $U(1)$ symmetry[d] and whose scalar potential satisfies certain dynamical constraints.

*Q* balls arise naturally in theories with supersymmetry. Supersymmetric extensions of the Standard Model, e. g., MSSM, predict the existence of new scalar baryons and leptons that have the requisite interactions that allow for *Q* balls.[5] Baryonic *Q* balls that form along a flat direction in the potential[6,7] can be entirely stable.[8]

In addition to scalar interactions, the scalar fields may have gauge interactions as well. This is the case in the MSSM, where the only scalar fields that carry a baryon number, squarks, transform nontrivially under the color $SU(3)$ gauge group. If the effect of the gauge fields cannot be eliminated, the semiclassical description of the solitons may be hampered by the complications related to confinement and other aspects of gauge dynamics. It is important, therefore, to design a proper description of nontopological solitons in the presence of gauge interactions. Previous treatments of supersymmetric *Q* balls have ignored the effects of the gauge fields because in many cases of interest it is sufficient to deal with the gauge-invariant scalar degrees of freedom.

A straightforward approach to *Q* balls in gauge theories would be to find a solution to the equations of motion with a fixed global charge. With the use of Hamiltonian formalism, the problem may be formulated as follows. Let the scalar fields $\phi$ be a representation (in general, reducible) of some semi-simple (unbroken) gauge group $G$ spanned by the generators $T^k$. And let the scalar potential $U(\phi)$ preserve a global $U(1)$ symmetry $\phi \rightarrow e^{iB\theta}\phi$, where $B$ is the $U(1)$ generator that is assumed to commute with $T^a$. To construct a $Q$-ball solution, one can find a minimum of the energy functional

$$E_{\text{total}} = \int d^3x \left[ \frac{1}{2}(E^a)^2 + \frac{1}{2}(H^a)^2 + p^\dagger p + |D_i\phi|^2 + U(\phi) \right] \tag{1}$$

 © 1998 American Institute of Physics

with an additional condition

$$\int d^3x\hat{B}\equiv\int d^3x\frac{1}{i}(p^\dagger B\phi-\phi^\dagger Bp)=Q. \tag{2}$$

In addition, the Gauss constraint must also be satisfied,

$$D_iE_i^a-\hat{T}^a=0. \tag{3}$$

Here $E^a$ ($H^a$) is a generic notation for the non-Abelian electric (magnetic) field, $D_\mu$ is a covariant derivative, the $p$ are the canonical momenta of the scalar fields, $p=\delta\mathcal{L}/\delta(D_0\phi)^\dagger=D_0\phi$, and the $\hat{T}^a$ are the non-Abelian charge densities,

$$\hat{T}^a\equiv\frac{1}{i}(p^\dagger T^a\phi-\phi^\dagger T^ap). \tag{4}$$

In general, such a solution can have a nonzero non-Abelian charge, with the gauge fields dying away slowly at infinity. It is unclear how to interpret such a solution in a theory with confinement of non-Abelian charge. It is also difficult to find such solutions by solving a complicated system of coupled nonlinear field equations.

In this note we formulate a set of simple sufficient conditions for the existence of $Q$-ball solutions that do not carry any overall non-Abelian charge (even though the charge densities may not vanish locally). For this type of nontopological solitons the issues of confinement are not essential, and the semiclassical description is valid.

Let us look for a minimum of functional (1), at which all gauge fields are taken to be zero, with additional conditions (2) and (3). If the energy of a configuration found this way is less than the energy of a collection of free scalar particles with the same charge $Q$, then a $Q$ ball does exist. A field configuration that minimizes the energy over a subspace of classical trajectories with zero gauge fields may not, of course, be the global minimum of energy, nor is it necessarily a solution of the equations of motion. Clearly, a conditional minimum of energy $E$ over a subset of configurations is greater or equal to the global minimum over the whole functional space. If the former is less than the energy of a free-particle state, then so is the latter. By construction, $Q$ balls of this type have zero gauge charges.

In order to formulate the sufficient conditions, we introduce the Lagrange multipliers $\lambda$ and $\xi^a$ that correspond to the constraints (2) and (3) (the latter is simply $\hat{T}^a(x)=0$ now), respectively, and reduce the problem to that of finding an extremum of

$$\mathcal{E}_{\lambda,\xi}=\int d^3x[p^\dagger p+|\partial_i\phi|^2+U(\phi)]-\lambda\left[\int d^3x\hat{B}(x)-Q\right]-\int d^3x\xi^a(x)\hat{T}^a(x). \tag{5}$$

The equation of motion for $p$ gives

$$p(x)=-i\lambda B\phi-i\xi^a(x)T^a\phi. \tag{6}$$

The equations for $\lambda$ and $\xi$ are

$$\lambda\phi^\dagger BT^a\phi+\xi^b\phi^\dagger\frac{1}{2}\{T^a,T^b\}\phi=0,\quad a=1,\ldots,\dim(G), \tag{7}$$

$$\int d^3x[\lambda\phi^\dagger B^2\phi+\xi^b(x)\phi^\dagger BT^b\phi]=Q. \tag{8}$$

A $Q$ ball exists if the system of equations (7) and (8) has a solution and if the corresponding extremal value of $\mathcal{E}_{\lambda,\xi}$ is less than the energy of any free-particle state with the same charge:

$$\mathcal{E}_{\lambda,\xi}<Q\min_i\{m_i/b_i\}, \tag{9}$$

where $m_i$ is the mass of the $i$th particle, which has the global charge $b_i$.

It is easy to see that the energy of a soliton can be found from the minimization of a functional without the conjugate momenta,

$$E_\lambda=\int d^3x[|\partial_i\phi|^2+\hat{U}_\lambda(\phi)], \tag{10}$$

where

$$\hat{U}_\lambda(\phi)=U(\phi)-\lambda[\lambda\phi^\dagger B^2\phi+\xi^a(\lambda,\phi)\phi^\dagger BT^a\phi], \tag{11}$$

and the $\xi^a(\lambda,\phi)$ are found from the system of equations (7). As in Refs. 2 and 9, one can use the correspondence between a $Q$ ball in the potential $U(\phi)$ and a bounce in $d=3$ Euclidean dimensions in the potential $\hat{U}_\lambda(\phi)$.

These conditions simplify in the thin-wall limit, where one can approximate the $Q$ ball solution by a field configuration that vanishes outside a sphere with radius $R$, and is $\phi(x)=e^{-i(\lambda B+\xi T)t}\phi_0$ for $|\mathbf{x}|<R$. If one defines $\overline{\lambda}=2V\lambda/Q$ and $\overline{\xi^a}=2V\xi^a/Q$, where $V=4\pi R^3/3$, equations (7) and (8) become a system of linear equations for $\overline{\lambda}$ and $\overline{\xi}$. It has a solution if there exists a gauge-invariant polynomial of $\phi$ and $\phi^\dagger$ with a nonzero baryon number (cf. Ref. 10). The condition of stability of a $Q$ ball with respect to its decay into the free scalar particles becomes

$$\min_{\phi_0}\sqrt{U(\phi_0)\overline{\lambda}(\phi_0)}\leqslant\min_i\{m_i/b_i\}. \tag{12}$$

For illustration, let us consider a scalar condensate associated with a $udd$ flat direction in the MSSM,[11] where the squarks $q_a^{(j)}$ have nonzero VEVs. A color-singlet condensate that satisfies equations (7) at $\xi^a=0$ can have the form $q_a^{(j)}=e^{i\lambda t/3}\varphi^{(j)}(x)\delta_a^j$. The constraints (7) are automatically satisfied for the off-diagonal generators of color $SU(3)$ (in the Gell-Mann basis). The remaining two equations for $T^3$ and $T^8$ demand that $\varphi^{(1)}\times(x)=\varphi^{(2)}(x)=\varphi^{(3)}(x)\equiv\phi(x)$. At the same time, the global $U_B(1)$ current $j_B^\mu(x)\equiv\frac{1}{3}q_a^{(j)\dagger}\overleftrightarrow{\partial}^\mu q_a^{(j)}=\frac{1}{3}\lambda\phi^2(x)\neq 0$. Of course, the vanishing of the gauge charge is automatic for every flat direction of the MSSM and need not be verified explicitly, thanks to the general theorems.[10] The remaining condition (9) is also satisfied as long as the scalar potential grows more slowly than the second power of the scalar VEV along the flat direction.

We have formulated the sufficient conditions for the existence of $Q$ balls in a class of gauge theories. Although the true ground state in the sector of fixed charge may have

nonvanishing gauge fields, its energy is less than that of the configuration we have constructed. The latter, in turn, is less than the energy of any free-particle state with the same global charge, which ensures the existence of a soliton.

We thank A. Cohen and S. Dubovsky for discussions. P. T. thanks the Theory Division at CERN for hospitality. The work of P. T. is supported in part by CRDF Grant RP1-187.

[a)]e-mail: Alexander.Kusenko@cern.ch
[b)]e-mail: mshaposh@nxth04.cern.ch
[c)]e-mail: peter@flint.inr.ac.ru
[d)]The conservation of a local $U(1)$ charge[3] or a global non-Abelian charge[4] can also lead to the appearance of nontopological solitons.

[1] G. Rosen, J. Math. Phys. **9**, 996 (1968); R. Friedberg, T. D. Lee, and A. Sirlin, Phys. Rev. D **13**, 2739 (1976).
[2] S. Coleman, Nucl. Phys. B **262**, 263 (1985).
[3] G. Rosen, J. Math. Phys. **9**, 999 (1968); K. Lee, J. A. Stein-Schabes, R. Watkins, and L. M. Widrow, Phys. Rev. D **39**, 1665 (1989).
[4] A. M. Safian, S. Coleman, and M. Axenides, Phys. Rev. D **297**, 498 (1988).
[5] A. Kusenko, Phys. Lett. B **405**, 108 (1997).
[6] G. Dvali, A. Kusenko, and M. Shaposhnikov, Phys. Lett. B **417**, 99 (1998).
[7] K. Enqvist and J. McDonald, http://xxx.lanl.gov/abs/hep-ph/9711514
[8] A. Kusenko and M. Shaposhnikov, Phys. Lett. B, in press;http://xxx.lanl.gov/abs/hep-ph/9709492.
[9] A. Kusenko, Phys. Lett. B **404**, 285 (1997).
[10] F. Buccella, J. P. Derendinger, S. Ferrara, and C. A. Savoy, Phys. Lett. B **115**, 375 (1982); I. Affleck, M. Dine, and N. Seiberg, Nucl. Phys. B **241**, 493 (1984); **256**, 557 (1985); M. A. Luty and W. Taylor, Phys. Rev. D **53**, 3399 (1996).
[11] T. Gherghetta, C. Kolda, and S. P. Martin, Nucl. Phys. B **468**, 37 (1996).

Published in English in the original Russian journal. Edited by Steve Torstveit.

# Matrix element of the anomalously low-energy ($3.5\pm0.5$ eV) transition in $^{229}$Th and the isomer lifetime

A. M. Dykhne
*Troitsk Institute of Innovational and Thermonuclear Studies*

E. V. Tkalya[a)]
*Scientific-Research Institute of Nuclear Physics, M. V. Lomonosov Moscow State University, 119899 Moscow, Russia*

(Submitted 30 December 1997)
Pis'ma Zh. Éksp. Teor. Fiz. **67**, No. 4, 233–238 (25 February 1998)

The matrix element of the anomalously low-energy ($3.5\pm0.5$ eV) nuclear $M1$ transition between the first excited state and the ground state of the $^{229}$Th nucleus is determined with allowance for the Coriolis mixing of the rotational bands. The upper and lower limits on the lifetime of the level with respect to an isomeric transition are given. A method is proposed for measuring the half-life of the low-lying isomer $^{229m}$Th directly in a $^{233}$U sample. © *1998 American Institute of Physics.* [S0021-3640(98)00204-7]

PACS numbers: 23.20.Lv, 27.90.+b, 21.10.Tg

It has been known for about eight years that $^{229}$Th possesses an anomalously low-lying nuclear level with energy $\leqslant 5$ eV.[1] In 1994 it was established on the basis of an analysis of measurements of the energies of $\gamma$ transitions to the ground and first excited states in $^{229}$Th that the energy of this level lies in the range $3.5\pm1.0$ eV.[2] There is virtually no doubt that this low-lying state (we shall designate it as $|is\rangle$) possesses spin $J^{\pi}=3/2^{+}$ and is the bandhead of the rotational band $K^{\pi}[Nn_z\Lambda]=3/2^{+}[631]$, where $K[Nn_z\Lambda]$ are the asymptotic quantum numbers in the Nilsson model.

The first direct observation of a nuclear isomeric transition in $^{229}$Th at optical energy has recently been reported.[3] Radiation corresponding to a direct nuclear transition with energy $\omega_N=3.5\pm0.5$ eV from a low-lying isomeric level to the ground state was observed, as was radiation at 2.3–2.5 eV, which is attributed to the predicted[4] isomeric decay of the nuclear level $3/2^{+}(3.5\pm0.5$ eV) via an electron bridge. Unfortunately, the authors were unable to measure the half-life of the $3/2^{+}$ level. We shall show below that this is possible to do with an improved version of the apparatus used in Ref. 3.

Determining the lifetime is not the only requirement for making further progress in the study of the properties of the $3/2^{+}(3.5\pm0.5$ eV) state. It is of interest to excite a large number of $^{229m}$Th nuclei by radiation from a laser or a special lamp.[5] This would make it possible to produce a population inversion on nuclear levels, to develop a nuclear metrological light source, and to search for $\alpha$ decay of the low-lying state, the probability and spectrum of which were predicted in Ref. 6.

 © 1998 American Institute of Physics

To design such experiments it is necessary to have an idea of the cross sections of the processes and the lifetime of the $3/2^+(3.5\pm0.5$ eV) level. For this it is in turn necessary to know the nuclear matrix element of the isomeric transition. The ground state of the $^{229}$Th nucleus (which we designate as $|gr\rangle$) is the bandhead of the rotational band $5/2^+[633]$ (Ref. 7). For this reason the isomeric transition can be of multipole order $M1$ or $E2$. As was shown in Ref. 4, the $E2$ component can be neglected over a wide range of hindrance factors for the $M1$ or $E2$ transitions. The $M1$ transition between the $3/2^+[631]$ and $5/2^+[633]$ bands, with the asymptotic quantum number $\Lambda$ changing by 1, is forbidden and should be weak.

A transition similar to the one investigated is known to occur in $^{233}$U nuclei. There the reduced probability $B_{\text{W.u.}}$ of the $M1$ transition $3/2^+3/2[631](312.17$ keV) $\rightarrow 5/2^+5/2[633](0.0)$ in Weisskopf units equals 0.0030.[8] At the same time, the value of $B_{\text{W.u.}}(M1)$ in the Nilsson model (the matrix elements are calculated in Ref. 9) is more than an order of magnitude larger than the experimental value. A similar situation may occur in $^{229}$Th as well. For this reason, we shall estimate the desired quantity $B(M1;3/2^+3/2[631]\rightarrow 5/2^+5/2[633])$ for the $^{229}$Th nucleus on the basis of the existing experimental data rather than model calculations.

Thus far only one $M1$ transition between the bands $3/2^+[631]$ and $5/2^+[633]$ has been measured in $^{229}$Th — this is the 25.3 keV transition between the states $9/2^+5/2[633](97.13$ keV) and $7/2^+3/2[631](71.82$ keV). Its reduced probability was determined in Ref. 10 $B(M1;9/2^+\rightarrow 7/2^+)=(0.032\pm0.006)\mu_N^2=(1.8\pm0.3)\times10^{-2}$ W.u., where $\mu_N=e/2M$ is the nuclear magneton (here and below we use units with $\hbar=c=1$). These data are sufficient to find $B(M1;3/2^+3/2[631]\rightarrow 5/2^+5/2[633])$ in the case when the Coriolis interaction between the bands of interest is not very strong.

In the familiar situation (see, for example, Ref. 11) the amplitudes of the interband $\gamma$ transitions in nuclei are given mainly by the Alaga pure rotation relations. From this standpoint, all the existing experimental data for the ground band $5/2^+[633]$ in $^{229}$Th and the band $3/2^+[631]$ coupled to it attest to the fact that the Coriolis interaction of these two bands is relatively weak.[10,12] Here the bands exhibit a pronounced rotational structure, the series expansions of the energies of the levels converge rapidly,[10,12] and the intensities of the $\alpha$ transitions to levels of the $3/2^+[631]$ band as a result of $\alpha$ decay of the $^{233}$U$(5/2^+5/2[633])$ ground state are only slightly higher than for the analogous levels of the ground band,[12] and so on. Moreover, analysis of the reduced probabilities of the three measured $M1$ $\gamma$ transitions between these bands in $^{233}$U (see Ref. 8), viz., $3/2^+3/2[631](312.17$ keV$)\rightarrow 5/2^+5/2[633](0.0)$, $5/2^+3/2[631](340.68$ keV$)\rightarrow 7/2^+5/2[633](0.0)$, and $5/2^+3/2[631](340.68$ keV$)\rightarrow 7/2^+5/2[633](40.35$ keV), shows good agreement (to within the accuracy of the measurements) Alaga pure rotation relations. This also holds for the relative intensities of two $M1$ transitions from the $5/2^+5/2[633](236.25$ keV) state to the $5/2^+3/2[631](179.75$ keV) and $3/2^+3/2[631]$ $\times(149.96$ keV) states in $^{225}$Ra (Ref. 13). There are no other measured $M1$ transitions between the rotational bands $3/2^+[631]$ and $5/2^+[633]$.

On this basis, we shall first estimate the relevant reduced probability $B(M1;3/2^+3/2[631](3.5$ eV$)\rightarrow 5/2^+5/2[633](0.0))$ in $^{229}$Th according to the Alaga pure rotation relations for transitions of the same multipole order between different states of two rotational bands. To underscore the fact that we are talking about the ''zeroth'' approximation we employ the notation $B^{(0)}(M1)$. Taking as the initial value the value of

$B(M1;9/2^+5/2[633]\rightarrow 7/2^+3/2[631])$ from Ref. 10, we immediately obtain

$$B^{(0)}(M1)=(0.069\pm 0.013)\mu_N^2=(3.8\pm 0.7)\times 10^{-2}\text{W.u.} \tag{1}$$

Let us now examine the corrections introduced by the Coriolis interaction. As result of this interaction there appear in the wave functions (WFs) of the nuclear states admixtures of states belonging to a neighboring band (here $|\Delta K|=1$) with the same angular momentum $I$. In consequence, for example, the $E2$ interband transition $9/2^+5/2[633]$ $\times$(97.13 keV)$\rightarrow 5/2^+3/2[631]$(29.19 keV), which is forbidden in terms of the asymptotic quantum numbers, has a relatively high reduced probability of 5 W.u. (Ref. 10). We are interested mainly in how an admixture of the $5/2^+3/2[631]$(29.19 keV) state to the ground state of $^{229}$Th changes the value of $B^{(0)}(M1)$. A detailed exposition of the theory of the Coriolis interaction in application to nuclear levels can be found in the monograph Ref. 11. For this reason, we shall retain the notation adopted there, giving explanations only where absolutely necessary.

We write the matrix element of the $M1$ transition between the bands $K_i=3/2$ and $K_f=5/2$, taking into account in the internal moment operators the terms that are linear in $I_\pm$ (Ref. 11):

$$\langle K_fI_f\|\mathcal{M}(M1)\|K_iI_i\rangle=\sqrt{2I_i+1}C^{I_fK_f}_{I_iK_i11}(M_1+M_2[I_f(I_f+1)-I_i(I_i+1)]). \tag{2}$$

Here $C^{I_fK_f}_{I_iK_i11}$ is a Clebsch–Gordan coefficient and $M_1$ and $M_2$ are matrix elements. For the time being, we are forced to treat the matrix element $M_1$ as a free parameter. The matrix element $M_2$ can be calculated from the experimental data. In the expression

$$M_2=\frac{1}{\sqrt{2}}\langle K_f|[\varepsilon_{+1},\mathcal{M}(M1,\nu=0)]|K_i\rangle \tag{3}$$

the brackets denote a commutator, $\nu$ is a tensor index in the internal (tied to the nucleus) coordinate system, and $\langle K_f|\varepsilon_{+1}|K_i\rangle$ is the well-known parameter determining the magnitude of the band mixing (see Ref. 11).

The matrix element $M_2$ can be expressed in terms of the transition moments inside the bands as

$$M_2=\frac{1}{\sqrt{2}}\langle K_f|\varepsilon_{+1}|K_i\rangle(\langle K_i|\mathcal{M}(M1,\nu=0)|K_i\rangle-\langle K_f|\mathcal{M}(M1,\nu=0)|K_f\rangle), \tag{4}$$

and the latter can in turn be calculated in terms of the effective $g$ factors — the rotational gyromagnetic ratio $g_R$ and the internal gyromagnetic ratio $g_K$: $\langle K|\mathcal{M}(M1,\nu=0)|K\rangle$ $=\sqrt{3/4\pi}(g_K-g_R)K\mu_N$. For the ground band $5/2^+[633]$ in $^{229}$Th one has $g_R=0.309$ $\pm 0.016$ and $g_K=+0.128\pm 0.017$ (Ref. 10). For the $3/2^+[631]$ band the value $|g_K-g_R|=0.58\pm 0.09$ was found in Ref. 12. We can ascertain the sign of the expression within the absolute value signs. For an unpaired neutron $g_K\cdot K\approx 0.6g_n^{(s)}\langle\varphi_K|s_3|\varphi_K\rangle$. The spin gyromagnetic ratio is $g_n^{(s)}=-3.8263$ and the spin matrix element with respect to the WFs of the internal motion in the Nilsson model was calculated in Ref. 9 as $\langle\varphi_K|s_3|\varphi_K\rangle\approx 0.15$. Therefore for this band $g_K-g_R=-0.58\pm 0.09$ and $g_K\approx -0.29$, which agrees well with the estimate $-0.23$ based on the Nilsson model.

We find the quantity $\langle K_f|\varepsilon_{+1}|K_i\rangle$ from the reduced probability of the interband $E2$ transition $9/2^+5/2[633](97.13\ \text{keV})\rightarrow 5/2^+3/2[631](29.19\ \text{keV})$. In first order the Coriolis forces renormalize the internal operator $\mathcal{M}(E2,\nu=\pm 1)\rightarrow\mathcal{M}(E2,\nu=\pm 1)+\sqrt{15/8\pi}eQ_0\varepsilon_{\pm 1}$ (Ref. 11). We shall take the value $8.816e$ barn for the internal quadrupole moment $Q_0$ (Ref. 10). It is obvious that the high intensity observed in Ref. 10 for this forbidden (in terms of the asymptotic quantum numbers $n_Z$ and $\Lambda$) transition is mainly due to the additional part of the internal operator. Hence a simple calculation gives $\langle K_f|\varepsilon_{+1}|K_i\rangle=0.052$.

On the basis of these estimates it is easy to show from Eqs. (3) and (4) that $M_2=-0.8\times 10^{-2}\mu_N$. Using Eq. (2) the modulus of the matrix element $M_1$ can be recovered from the reduced probability of the measured $M1$ transition $9/2^+5/2[633](97.13\ \text{keV})\rightarrow 7/2^+3/2[631](71.82\ \text{keV})$, while the sign can be determined by comparing with calculation according to the formula $\langle f|\mathcal{M}(M1)|i\rangle=\sqrt{3/4\pi}((g_K-g_R)\langle f|s_+|i\rangle+(g_l-g_R)\langle f|l_+|i\rangle)$ in the Nilsson model. The result is $M_1=0.33\mu_N$.

Now we can calculate the needed value of the reduced probability of an $M1$ transition from a low-lying level to the ground state. Substituting into Eq. (2) the computed matrix elements $M_1$ and $M_2$, we find $B(M1)$ as

$$B(M1;3/2^+3/2[631]\rightarrow 5/2^+5/2[633])=0.086\ \mu_N^2=4.8\times 10^{-2}\ \text{W.u.} \tag{5}$$

The magnetic moment of the isomeric level $3/2^+(3.5\ \text{eV})$ can be easily determined from the relation $\mu=g_RK+(g_K-g_R)K^2/(I+1)$. It was found that $\mu_{\text{is}}\approx -0.076\mu_N$, i.e., it has a different sign from and is much smaller in magnitude than the magnetic moment of the ground state $\mu_{\text{gr}}=0.45\mu_N$.

Comparing the values of $B(M1)$ from Eqs. (1) and (5) shows that the small mixing of the bands as a result of the Coriolis interaction increases the probability of the isomeric $M1$ transition by approximately a factor of 1.2–1.3.

Let us now estimate the lifetime $T_{1/2}^{\text{is}}$of the low-lying state. The upper limit is determined by the width of the radiative nuclear transition. For the most probable (according to the plots given in Ref. 3) value of the energy $\omega_N=3.7$ eV and for the reduced probability $B_{\text{W.u.}}(M1)$ from Eq. (5), the lifetime $T_{1/2}^{\text{is}}$ equals about 2.5 h. The real lifetime of the isomeric level will be shorter because of the existence of an electron bridge (EB). Thus, in sample No. 2 from Ref. 3, where, as estimated by the authors, the probability of the EB is approximately four times higher than that of a direct nuclear emission, the lifetime of the $3/2^+(3.5\pm 0.5\ \text{eV})$ state was about 30 min. In sample No. 1, where the probabilities of an EB and direct nuclear emission were found to be comparable, the lifetime was apparently $\approx 1$ h.

It is more difficult to determine the minimum possible lifetime of the $3/2^+(3.5\pm 0.5\ \text{eV})$ state. Let us consider first the case of an unexcited atom or molecule, when the conversion decay channel is closed because the ionization potential $I_0$ is greater than $\omega_N$. The probability of decay via an EB is maximum in the case when the energy $\omega_N$ is in resonance with the energy of an atomic (or molecular) $M1$ transition from the ground state $|i\rangle$ of the Th atom (molecule). Then the complicated expression for the EB probability $W_{eb}$ factorizes and assumes the simple form (see, for example, Eq. (28) in Ref. 14):

$$W_{eb}\simeq\Gamma_n P_{INEET}, \tag{6}$$

where $\Gamma_n$ is the total width of the intermediate atomic or molecular state $|n\rangle$, in which excitation of the atom occurs with relative probability $P_{INEET}$ in a nonradiative decay of the isomeric nuclear level. (Here we are talking about the inverse of the NEET process (Nuclear Excitation by Electron Transition[14]), whence the letter I in INEET.) The relative probability can be calculated according to the formula[14]

$$P_{INEET} \simeq \frac{E_{\rm int}^2(M1;\omega_N;is\to gr,i\to n)}{(\mathcal{E}_n-\mathcal{E}_i-\omega_N)^2+(\Gamma_n+\Gamma_i+\Gamma_{\rm is})^2/4}, \tag{7}$$

where $E_{\rm int}$ is the electron–nuclear interaction energy in second-order perturbation theory and $\mathcal{E}_{i,n}$ is the binding energy in atomic shells.

In Eq. (6) the quantity $P_{INEET}$ cannot exceed 1 by definition, since it is the relative probability for the excitation of an atom per nuclear transition from an excited state to the ground state. The largest radiative widths $\Gamma_n$ for energies of 3–4 eV in the Th atom equal about $10^{-8}$ eV.[15] In the limit $P_{INEET}\to 1$ expression (7) gives a lower limit of $10^{-8}$ s for $T_{1/2}^{\rm is}$. In reality, however, resonance, though not excluded theoretically, is extremely unlikely. The atomic density of states in Th in the range of excitation energies 3–4 eV is about $10^2$ levels/eV.[15] For this reason, the detuning in the denominator in Eq. (7) is of the order of $10^{-2}$ eV. Calculations show that the square of the interaction energy has a maximum value of about $10^{-10}$ eV$^2$ for the atomic $M1$ transitions $7S_{1/2}\to 8S_{1/2},9S_{1/2}$. As a result, it should be expected that the minimum lifetime of the isomer in an atom is $\simeq 10^{-2}$ s. In the case of molecules, the density of excited states is much higher. However, the atomic wave functions through which the EB occurs have small amplitudes in the molecular orbitals. However, in each specific case there can be deviations in one direction or the other.

A very interesting case is that in which the atom or molecule is in a state whose excitation energy is greater than the difference $I_0-\omega_N$, and conversion decay of the $3/2^+(3.5\pm 0.5$ eV) state becomes allowed. Here the spectrum of lifetimes of the isomeric level is very wide and depends on the particular excited state in which the atom or molecule is found. The corresponding estimates were made in Ref. 4. For us it is important here that the decay via the internal electron conversion channel occurs over a fraction of a second, i.e., rapidly compared with the characteristic half-life for decay via the EB in the experiment of Ref. 3. This suggests the following experiment for determining the lifetime of the low-lying level in $^{229}$Th. A $^{233}$U target is irradiated for a short time by laser light with photon energy $\omega_L > I_0-\omega_N$ and with sufficient intensity. During the interaction with the laser pulse, decay by internal electron conversion from excited atomic levels occurs for a certain fraction of the $^{229m}$Th$(3/2^+,3.5\pm 0.5$ eV) nuclei, which are always present in a $^{233}$U sample in the proportion $\beta T_{1/2}^{\rm is}/T_{1/2}^U$, where $\beta=0.02$–$0.03$ is the probability of population of the isomeric state (branching ratio) in the $\alpha$ decay of $^{233}$U, which has a half-life of $T_{1/2}^U=1.592\times 10^5$ years. The current pulse of conversion electrons can serve as the conversion-decay signal. After irradiation the number of isomeric nuclei and their optical activity will recover in accordance with the law $1-\exp(-\lambda_{\rm is}t)$, where $\lambda_{\rm is}=\ln 2/T_{1/2}^{\rm is}$. Besides optical measurements, this process can be monitored by a different method in the case of a substantial decrease in the number of isomeric nuclei — by repeating the laser pulses in different, gradually increasing time intervals and measuring the conversion-electron current. This improvement of the experimental procedure of Ref.

3 will not only make it possible to measure $T_{1/2}^{is}$ but also to assert with much greater confidence that the observed radiation is due to a nuclear transition.

This work is supported in part by the Russian Fund for Fundamental Research (grants 96-02-16200a and 98-02-16070a), by a Grant from the State Science and Technology Program ''Physics of Quantum and Wave Processes,'' and by Grant 96-15-96481 in Support of the Leading Scientific Schools.

[a)]e-mail: tkalya@ibrae.ac.ru

---

[1] C. W. Reich and R. G. Helmer, Phys. Rev. Lett. **64**, 271 (1990).
[2] R. G. Helmer and C. W. Reich, Phys. Rev. C **49**, 1845 (1994).
[3] G. M. Irwin and K. H. Kim, Phys. Rev. Lett. **79**, 990 (1997).
[4] V. F. Strizhov and E. V. Tkalya, Zh. Éksp. Teor. Fiz. **99**, 697 (1991) [Sov. Phys. JETP **72**, 387 (1991)].
[5] E. V. Tkalya, V. O. Varlamov, V. V. Lomonosov, and S. A. Nikulin, Phys. Scr. **53**, 296 (1996).
[6] A. M. Dykhne, N. V. Eremin, and E. V. Tkalya, JETP Lett. **64**, 345 (1996).
[7] Y. A. Akovali, Nucl. Data Sheets **58**, 555 (1989).
[8] Y. A. Akovali, Nucl. Data Sheets **59**, 263 (1990).
[9] R. R. Chasman, I. Ahmad, A. M. Friedman, and J. R. Erskine, Rev. Mod. Phys. **49**, 833 (1977).
[10] C. E. Bemis, Jr., F. K. McGowan, J. L. C. Ford *et al.*, Phys. Scr. **38**, 657 (1988).
[11] A. Bohr and B. Mottelson, *Nuclear Structure*, W. A. Benjamin, Reading, Mass. [Russian translation, Mir, Moscow, Vol. 2, 1977].
[12] L. A. Kroger and C. W. Reich, Nucl. Phys. A **259**, 29 (1976).
[13] Y. A. Akovali, Nucl. Data Sheets **60**, 617 (1990).
[14] E. V. Tkalya, Zh. Éksp. Teor. Fiz. **102**, 379 (1992) [Sov. Phys. JETP **75**, 200 (1992)].
[15] C. Corliss and W. Bozeman, *Experimental Transition Probabilities for Spectral Lines of Seventy Elements*, U. S. Government Printing Office, Washington, D. C., 1962 [Russian translation, Mir, Moscow, 1968].

Translated by M. E. Alferieff

# Estimates of electron–positron pair production in the interaction of high-power laser radiation with high-$Z$ targets

D. A. Gryaznykh, Ya. Z. Kandiev, and V. A. Lykov[a)]
*All-Russia Scientific and Research Institute of Theoretical Physics Russian Federal Sciences Center, 456770 Snezhinsk, Russia*

(Submitted 12 January 1998)
Pis'ma Zh. Éksp. Teor. Fiz. **67**, No. 4, 239–244 (25 February 1998)

Electron–positron production processes occurring in the interaction of $10^{18}$–$10^{20}$ W/cm$^2$ laser radiation with high-$Z$ targets are examined. Computational results are presented for the pair production and the positron yield from the target with allowance for the contribution of pair production processes due to electrons and bremsstrahlung photons. Monte Carlo simulations using the PRIZMA code confirm the estimates obtained. The possible positron yield from high-$Z$ targets irradiated with $10^2$–$10^3$ TW laser radiation is estimated to be $10^9-10^{11}$.
© *1998 American Institute of Physics.* [S0021-3640(98)00304-1]

PACS numbers: 52.50.Jm, 25.30.Fj, 12.20.Ds

The possibility of electron–positron production by relativistic electrons accelerated by a laser field was discussed quite a long time ago.[1] It was estimated that the positron production efficiency can be high.[2] The papers cited considered the case of pair production during oscillations of electrons in an electromagnetic wave in the focal region of laser radiation. Here we examine a somewhat different pair production scenario.

The interaction of high-power laser radiation with matter results in the production of fast, high-temperature electrons.[3] Relativistic temperatures of fast electrons $T_f \approx 1$ MeV have been observed in experiments with high-power picosecond lasers.[4] Self-consistent electric fields confine these electrons in the target. When the electrons interact with the matter in a high-$Z$ target, electron–positron pairs are produced (see Ref. 5). The annihilation photon spectrum can be used for diagnostics of the electron–positron plasma.

In the present letter we make estimates of the positron and photon yields as functions of the laser power. We have made an assessment of the possibility of using high-power ($10^2$–$10^3$ TW) ultrashort-pulse lasers to produce a high-luminosity positron source. Such sources are required for the production of slow (1–10 eV) positrons with an intensity of $10^8$ positrons/s. Such positrons have wide applications for the study of Fermi surfaces, defects, and surfaces of materials.[6]

The interaction of relativistic electrons with matter can lead to electron–positron pair production in the following two processes:

(i) $e^- + Z \rightarrow 2e^- + e^+ + Z$;

 © 1998 American Institute of Physics

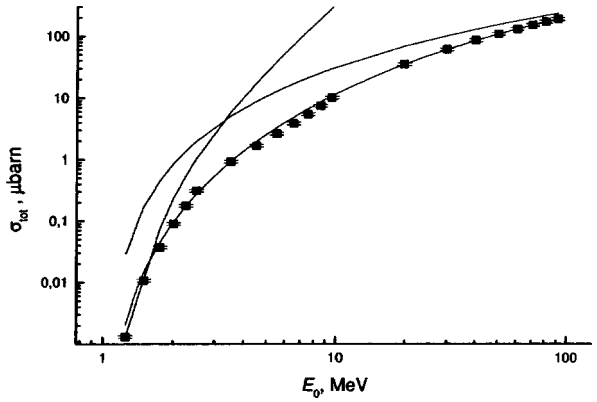


FIG. 1. Total cross section for electron–positron pair production by an electron in the Coulomb field of a $Z=1$ nucleus; numerical data, asymptotic expressions, and approximation formula.

(ii) $e^- + Z \to e + \gamma + Z \to 2e^- + e^+ + Z$.

In Ref. 7 analytical and numerical calculations of the total cross section of the pair electroproduction process are performed using the differential cross section.[8] According to this work the total cross section of the process (i) near the threshold equals

$$\sigma_{e\to 2ee^+} = \frac{7Z^2 r_e^2 \alpha^2}{2304} \frac{(E_0 - 2mc^2)^3}{(mc)^3}, \tag{1}$$

where $r_e$ is the classical electron radius, $\alpha = 1/137$, $mc^2$ is the electron mass, and $E_0$ is the kinetic energy of the initial electron. At high energies the cross section grows as[9]

$$\sigma_{e\to 2ee^+} = \frac{28\pi Z^2 r_e^2 \alpha^2}{27} \ln^3 E_0/mc^2. \tag{2}$$

The approximation formula

$$\sigma_{e\to 2ee^+} = 5.22 Z^2 \ln^3\left(\frac{2.30 + E_a[\mathrm{MeV}]}{3.52}\right) \mu\mathrm{b}. \tag{3}$$

describes both limits.

Figure 1 shows the points obtained by numerically integrating the exact formulas for the differential cross section,[7] the asymptotic cross sections (2) and (1), and a plot of the approximating function (3).

Let us examine the contribution of the process (i) to the electron–positron pair production in matter. Let us assume that the fast electrons produced when the high-intensity laser radiation interacts with matter are confined by self-consistent electric fields, so that electron stopping in the target can be treated just as in an infinite medium.

The probability of pair production during electron passage in matter with energy loss from $E_0$ to the threshold $2mc^2$ equals

$$w_e = \int_{2mc^2}^{E_0} \sigma_{e\to 2ee^+} \left(-\frac{dE}{dx}\right)^{-1} n_i dE, \tag{4}$$

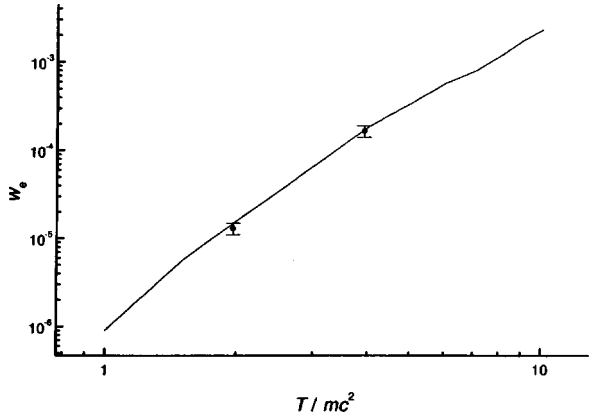


FIG. 2. Probability of positron production by an electron in the Coulomb field of a lead nucleus versus temperature. The data points show the PRIZMA simulation results.

where $\sigma_{e\to 2ee^+}$ is given by Eq. (3), $n_i$ is the ion density, and $dE/dx$ is the electron energy loss per unit path length.

Taking the Rohrlich–Carlsson formula[10] for $dE/dx$, we carried out a numerical computation of the integral in Eq. (4) for the case of lead. Averaging $w_e(E)$ over the relativistic Maxwellian distribution with temperature $T$, we obtained the number of positrons produced per initial electron versus temperature. This relation is shown in Fig. 2. Performing the same averaging with coefficient $E$, we obtained the average energy of the positrons produced.

The average positron energy determines the required thickness of the target, since the mean free path in matter depends on energy. For lead this dependence is determined by the formula[11]

$$\rho\Delta_{e^+}=\begin{cases}0.412|E|^{1.265-0.0954\ln E}, & 0.01\leqslant E\leqslant 3,\\ 0.53E-0.106, & 3<E<20,\end{cases} \tag{5}$$

where $[E]$ is given in MeV and $[\rho\Delta]$ in $\mathrm{g\cdot cm^{-2}}$. The positron mean free path in lead for different temperatures of the initial electrons is shown in Fig. 3.

Let us estimate the probability of pair production by bremsstrahlung photons (process (ii)). In contrast to the electrons confined in the target by the self-consistent electric field, photons can escape from the target. The cross section of the process $\gamma\to e^+e^-$ is tabulated in Ref. 11 (p. 267). Data on the incoherent photon absorption cross section $\sigma_{\alpha\mathrm{incoh}}$ can also be found there.

The probability of pair production by one photon with energy $\epsilon$ equals

$$w_\gamma(\epsilon)=w_\alpha\frac{\sigma_{\gamma\to e^+e^-}(\epsilon)}{\sigma_{\alpha\mathrm{tot}}(\epsilon)}, \tag{6}$$

where $\sigma_{\alpha\mathrm{tot}}(\epsilon)=\sigma_{\gamma\to e^+e^-}(\epsilon)+\sigma_{\alpha\mathrm{incoh}}(\epsilon)$, $w_\alpha(\epsilon)=1-\exp(-\sigma_{\alpha\mathrm{tot}}(\epsilon)n_i\Delta)$, and $\Delta$ is the thickness of the target. For an infinite target

$$w_\gamma^\infty=\sigma_{\gamma\to e^+e^-}/\sigma_{\alpha\mathrm{tot}}. \tag{7}$$

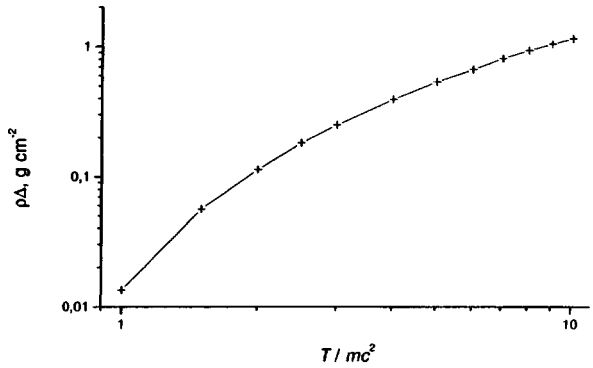


FIG. 3. Mean free path of positrons produced by an electron in lead versus temperature.

We take the photon spectrum in the form

$$dN/dE \simeq \epsilon_{e\to e\gamma} T^{-1} \exp(-\epsilon/T), \tag{8}$$

where $\epsilon_{e\to e\gamma} = 3\times 10^{-4} ZT/mc^2$ is the ratio of the total energy transferred to the bremsstrahlung photons to the total energy of the electrons and was determined in Sec. IV-20 of Ref. 12. Averaging $w_\gamma(\Delta,\epsilon)$ over the spectrum (8) we obtain

$$w_\gamma(\Delta,T) \simeq \epsilon_{e\to e\gamma} T^{-1} \int_{2mc^2}^{+\infty} \exp(-\epsilon/T) w_\gamma(\Delta,\epsilon)\, d\epsilon. \tag{9}$$

The dependence of the number of positrons produced by bremsstrahlung photons per initial electron versus temperature for an infinite slab and two thicknesses is presented in Fig. 4.

The results of the estimation of the number of positrons produced can be used to estimate the number of annihilation photons in targets with thickness greater than the

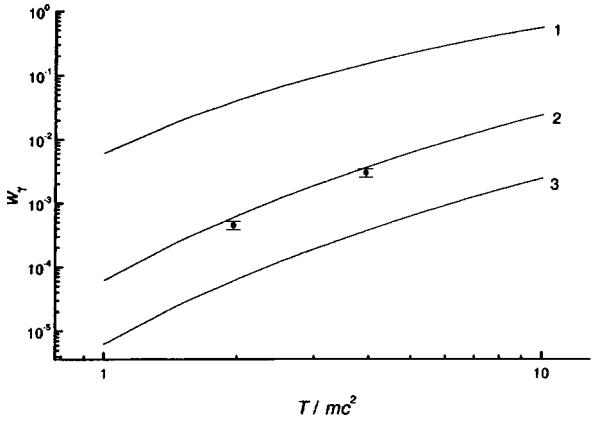


FIG. 4. Probability of positron production by an electron via bremsstrahlung photons in lead for thicknesses $\rho\Delta=\infty$ (curve *1*), $\rho\Delta=3$ g·cm$^{-2}$ (curve *2*), $\rho\Delta=0.3$ g·cm$^{-2}$ (curve *3*) versus temperature. The data points show the PRIZMA simulation results for a lead sphere of radius $\rho R=2.2$ g·cm$^{-2}$.

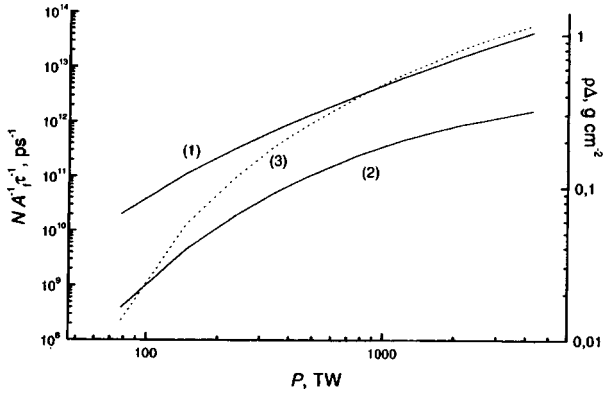


FIG. 5. Photon (*1*) and positron (*2*) yields $N/A_f\tau$ versus laser power. Curve *3* shows the optimum size of a target for a positron source.

positron mean free path (see Fig. 3) but less than the photon mean free path ($\approx 6$ g·cm$^{-2}$ for lead). The channel (ii) predominates here. For thickness 2–3 g·cm$^{-2}$ the photon yield reaches 0.04% per electron in a source with temperature $T \simeq 1$ MeV.

To check the estimates, calculations were performed using the PRIZMA code,[13] which simulates all basic electron, photon, and positron transport and production processes for any geometry (1D, 2D, and 3D) by the Monte Carlo method. The calculations were performed for a lead sphere with radius $R = 0.2$ cm and an electron source with temperature $T = 1$ and 2 MeV at the center. The results are presented in Figs. 2 and 4. They are in agreement with our estimates.

According to Ref. 3, the temperature of fast electrons which arise during the interaction of laser radiation with matter equals approximately

$$T_f \simeq mc^2[(1+0.7q_{18})^{1/2}-1], \tag{10}$$

where $q_{18}$ is the laser power density in $10^{18}$ W·cm$^{-2}$. When a laser pulse with energy $E_l$[J] and duration $\tau$[ps] is focused to a circle of diameter $d_f$[$\mu$m], the intensity equals $q_{18} = 400E_l/\pi d_f^2\tau$. The number of electrons produced equals $N_e = A_f E_l/\langle E_f\rangle$, where $A_f$ is the efficiency of conversion of laser radiation to fast electrons, and $\langle E_f\rangle$ is the average energy of the fast electrons.

We propose a sphere of finite density as a target into which the laser radiation is focused.[14] Such a target gives $A_f \approx 0.3$, high luminosity, and isotropic positron and photon yields. The target material should have a high atomic number $Z$, and the optimal diameter of the target is determined by the problems of the experiment and by the laser power.

To detect annihilation photons the size of the target was chosen to be $\rho R \approx 2-3$ g·cm$^{-2}$. The annihilation-photon yield $N_\gamma$ divided by $A_f$ and $\tau$ versus laser power is shown in Fig. 5. The diameter of the focal spot equals $d_f = 30$ $\mu$m. The photon yield reaches $10^{10}$–$10^{12}$ for a $10^2$–$10^3$ TW picosecond laser.

The positron yield from the target can be estimated as

$$N_+ \simeq N_e \frac{\rho\Delta_{e^+}}{\rho\Delta_{e^+}+\rho\Delta}\left(w_e + w_\gamma^\infty \frac{\rho\Delta}{\rho\Delta_\gamma}\right). \quad (11)$$

Here $\Delta_{e^+,\gamma}$ are the positron and photon mean free paths. The target for positron production must be of the order of $\Delta_{e^+}$ in size (see Fig. 3). The positron yield $N_+$ divided by $A_f$ and $\tau$ is plotted versus the laser power in Fig. 5. The dotted line in this figure shows the optimal target size $\rho\Delta$ for such an experiment. The positron yield reaches $10^9$–$10^{11}$ for $10^2$–$10^3$ TW picosecond laser.

Since the target is smaller in size than existing positron sources, the laser positron source can have a very high luminosity. The efficiency of conversion of fast positrons (MeV) to slow positrons (1–10 eV) can reach $10^{-2}$ (Ref. 15). Therefore, to produce a quasistationary source of slow positrons with an intensity of $10^8$ particles/s requires a laser with an energy of 10–30 J in a 10–30 fs pulse with a repetition frequency of 10–30 Hz. Undoubtedly, such a source would be useful for fundamental and applied investigations in solid-state physics, chemistry, and biology.

V. L. thanks Professor H. Hora for his interest in this work and for a helpful discussion. This work was supported by the International Science and Technology Center, Project 107-94.

[a)]e-mail: lyk@nine.ch70.chel.su

[1] J. W. Shearer *et al.*, in *Laser Interactions and Related Plasma Phenomena*, Vol. 3B, edited by H. Hora and G. H. Miley, Plenum Press, New York, 1974, p. 803; H. Hora, *ibid.*, p. 819.
[2] W. Becker, Laser Part. Beams **9**, 603 (1991).
[3] S. C. Wilks, W. L. Kruer, M. Tabak, and A. B. Langdon, Phys. Rev. Lett. **69**, 1383 (1992).
[4] K. Whaton, Y. Zakharenkov, B. A. Hammel *et al.*, ''Experimental investigation of laser matter interaction at $10^{20}$ W/cm$^2$,'' Report at 24th LCLIM, Madrid, Spain, June 3–7, 1996.
[5] E. P. Liang, in *Laser Interaction and Related Plasma Phenomena*, AIP Conf. Proc., Am. Inst. Phys., New York, 1993, p. 318.
[6] M. J. Puska and R. M. Nieminen, Rev. Mod. Phys. **66**, 841 (1994).
[7] D. A. Gryaznykh, Yad. Fiz. (in press).
[8] V. N. Baĭer and V. S. Fadin, Zh. Éksp. Teor. Fiz. **61**, 476 (1971) [Sov. Phys. JETP **34**, 253 (1972)].
[9] L. Landau and E. Lifchiz, Sow. Phys. **6**, 244 (1934).
[10] A. F. Akkerman, *Simulation of Charged-Particle Trajectories in Matter* [in Russian], Énergoatomizdat, Moscow, 1991, p. 35.
[11] O. F. Nemets and Yu. V. Gofman, *Handbook of Nuclear Physics* [in Russian], Naukova Dumka, Kiev, 1975.
[12] H. W. Koch and J. W. Motz, Rev. Mod. Phys. **31**, 920 (1959).
[13] Ya. Kandiev and V. Plokhoĭ, Vopr. At. Nauki Tekh., Metod. Programmy (Kharkov) **2**, 70 (1993).
[14] V. A. Lykov, V. E. Chernyakov, Ya. Z. Kandiev *et al.*, in *X-Ray Lasers*, edited by S. Svanberg and C. G. Wahlstrom, No. 151 of Institute of Physics Series, Institute of Physics Press, Philadelphia, 1996, p. 480.
[15] P. J. Schultz and K. G. Lynn, Rev. Mod. Phys. **60**, 701 (1988).

Translated by M. E. Alferieff

# Contact scanning near-field optical microscopy

D. A. Lapshin, S. K. Sekatskiĭ,[a)] and V. S. Letokhov
*Institute of Spectroscopy, Russian Academy of Sciences, 142092 Troitsk, Moscow Region, Russia*

V. N. Reshetov
*Moscow Engineering-Physics Institute, 115409 Moscow, Russia*

(Submitted 6 January 1998)
Pis'ma Zh. Éksp. Teor. Fiz. **67**, No. 4, 245–250 (25 February 1998)

A new method of scanning in near-field optical microscopy, which makes it possible to operate in contact with the experimental sample, is proposed and implemented. This method permits the practical utilization of the idea of using the dipole–dipole resonance transfer of excitation energy from the active element of the microscope to the sample for achieving a fundamental improvement in the resolution of near-field optical microscopy. © *1998 American Institute of Physics.* [S0021-3640(98)00404-6]

PACS numbers: 07.79.Fe

It was recently proposed[1] that the resolution in scanning near-field optical microscopy (SNOM) could be improved fundamentally by utilizing the Förster (dipole–dipole) resonance transfer of electronic excitation energy (fluorescence resonance energy transfer — FRET) from single fluorescing centers located on the tip of a ''light source'' (the active element of the microscope) to the experimental sample. In this approach the spatial resolution is determined not by the size of the light source (20–100 nm[2,3]), but rather by the Förster resonance energy transfer length $r_0$, which typically equals 1–5 nm (see, for example, the review in Ref. 4). Moreover, since the energy transfer efficiency is close to 1 if the donor–acceptor distance is less than $r_0$, the sensitivity of the proposed FRET microscope should also be better than that of a conventional near-field optical microscope.

To implement this method of microscopy the active element of the microscope must be scanned at a distance less than $r_0$ from the surface being examined, i.e., virtually in contact with it. This makes it impossible to use the well-developed shear-force methods widely used in SNOM practice for monitoring the microscope–sample distance, since both the distance range and the amplitude of the lateral oscillations of the tip in this case amount to several tens of nanometers[2,3] and are much larger than $r_0$. It is also impossible to use contact the methods widely employed in ''classical'' atomic-force microscopy, since these methods are, as a rule, based on the use of very compliant cantilevers, which cannot be used for scanning the quite massive fiber tips or heavy tips of other types, as is necessary in order to implement the proposed method of FRET microscopy.[5] Therefore, it is necessary to develop a new method of probe microscopy. This is made all the more

 © 1998 American Institute of Physics

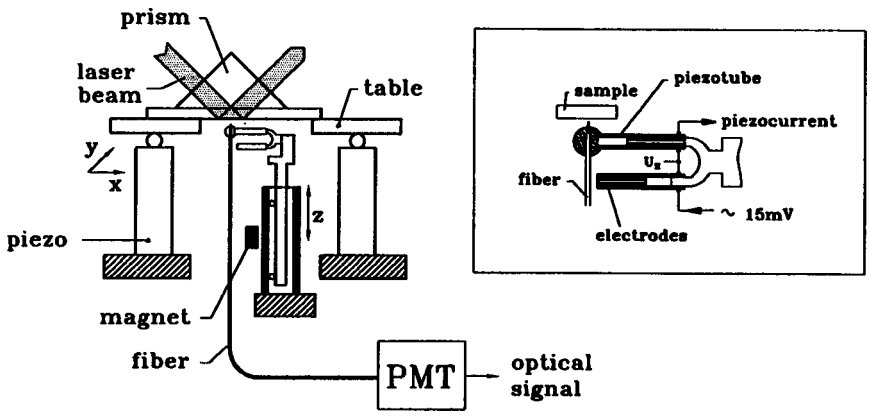


FIG. 1. Layout of a scanning photon tunneling microscope operating in the contact mode. Inset: More detailed diagram of the contact piezoelectric sensor to which the sharpened end of the optical fiber is secured.

timely by the fact that we recently demonstrated in practice tips that contain single fluorescing centers near the apex (so far we have used $F_2$ color centers at the ends of LiF tips[6,7]).

In the present letter we report the implementation of a new contact method for monitoring the distance to the experimental sample. The method is suitable for FRET microscopy. Of course, it can also be used in other fields of scanning microscopy.

The general layout of the photon scanning tunneling microscope (PSTM) used in the present work is shown in Fig. 1. We employed a similar scheme previously to investigate light scattering by a reflecting phase grating in the near-field region.[8] Basically (except for the piezoelectric contact sensor; see below) it is identical to the conventional PSTM scheme,[2,3] and we shall not discuss it in detail. The experimental sample consisted of a thin glass plate, on one side of which a reflecting phase grating was produced lithographically, i.e., nickel strips 3 $\mu$m wide and 40 nm high were deposited with a period of 10 $\mu$m. The sample is illuminated through a prism located at the top by He–Ne laser radiation under conditions of total internal reflection; when the sharpened end of the fiber is brought up to the sample to a distance of less than or of the order of the wavelength of the light, the conditions of total internal reflection break down, and light energy is transferred into a mode propagating in the fiber and is detected with a photomultiplier, to whose input the opposite end of the fiber is attached.

The fine engagement of the tip with the surface and the maintenance of contact between them during scanning are accomplished with a piezoelectric contact sensor consisting of two small piezoelectric cylinders (6 mm long, 1.3 mm in diameter), which are secured on a common base and form a tuning-fork type of resonator (see inset in Fig. 1). The sharpened point of the fiber was glued, using phenyl salicylate, to one of the piezoelectric cylinders so that only a very short (of the order of 0.1 mm long) tip of the fiber remained free. (Such a short length of the free end of the fiber was necessary in order to ensure adequate rigidity of the system; see below.) The internal electrodes of both piezoelectric tubes were grounded, while the external electrodes were split into two parts. The parts of the electrodes directed inward into the tuning fork were in electrical contact. One

piezoelectric tube was excited electrically by applying to its outer electrode a voltage at the frequency of the resonance oscillations, which in our case was equal to 13 kHz. Since the other piezoelectric tube is coupled with the first one by means of the common base and is in good acoustical contact, it is excited acoustically, which results in the appearance of a current and voltage, which are produced by the direct piezoelectric effect, on its electrodes.

In the absence of contact between the tip point and the sample, both the tip and the piezoelectric cylinders execute free oscillations in a direction normal to the surface being examined. In the typical case, when the amplitude of the control voltage equals 15 mV, the amplitude of these oscillations equals 7–8 nm (estimated on the basis of the piezoelectric constants and the Q factor ($Q \simeq 30$) of the corresponding oscillatory circuit, all of which we measured beforehand). When contact is made, the amplitude of the oscillations (and therefore also the piezoelectric voltage) changes. We employed the corresponding changes in the feedback circuit of the microscope when scanning the sample in the horizontal plane — by maintaining a constant amplitude within the the indicated range during scanning, one can trace the profile of the surface of interest much as in a ''classical'' atomic-force microscope.

We note that in reality we employed a somewhat more complicated scheme than that described above to record the changes in the piezoelectric voltage. Specifically, we used a self-excited oscillator scheme to excite resonance oscillations of the tuning fork. In this scheme, the corresponding oscillatory circuit is part of the electric oscillator, so that when contact is made, not only the amplitude but also the frequency of the resonance oscillations changes, and both channels (both amplitude and frequency) can be used in the feedback circuit of the microscope. The frequency channel was not used in the experiments described below, and it will not be discussed in detail. Additional information about piezoelectric sensors of this type and the mechanisms by which they interact with the surface are discussed in Ref. 9.

Figure 2 shows both topographic (a) and optical (b) images of the same section of the reflecting phase grating under study. No preprocessing or filtering were performed. A fragment of one of the metal strips of the grating, appearing as a dark (opaque) strip in the optical image and as a bright (elevated) strip in the topographic image, can be seen in both images. The spatial resolution for images of both types can be estimated as $\sim 0.5$ $\mu$m. This value can be attributed to inadequate sharpness of the fibers employed and is not important for the purpose of illustrating the principles of the new method of scanning near-field optical microscopy.

The engagement curves (curves of the detected signal versus distance) are displayed in Fig. 3. One can see from the curve c, which refers to the topographic channel, that the amplitude of oscillations of the tip remains unchanged right up until tip–surface contact, after which it decreases rapidly to 10% of the initial value as the sensor undergoes a vertical displacement of 360 nm. The corresponding vertical displacement of a similar sensor to which a massive tetrahedral diamond tip is secured is much smaller — for diamond tips the entire engagement curve, similar to the curve c, occupies a region of 10 nm. This is due to the fact that as the base of the fiber tip moves toward the surface, the fiber is not only compressed but it also bends, as one would expect for a long, thin rod which is slightly inclined with respect to the surface (which always happens in reality).[10] After coming into contact with the surface, the end of the tip no longer pulls away from

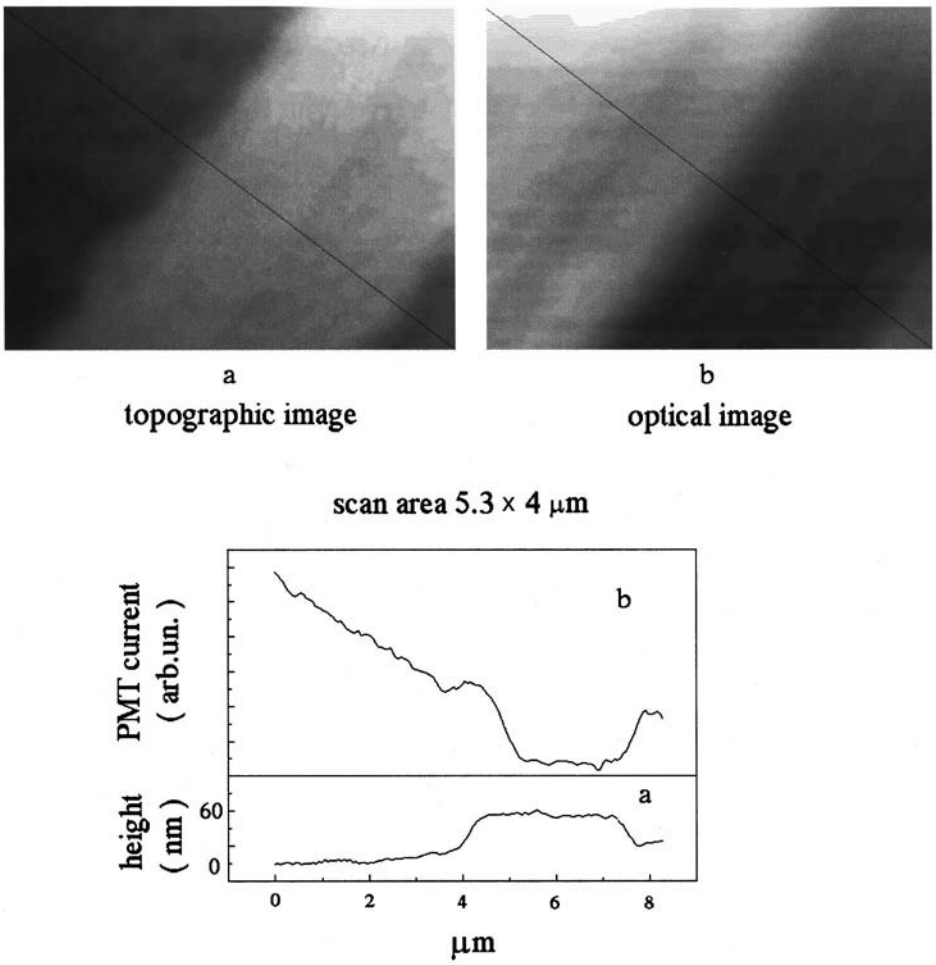


FIG. 2. Topographic (a) and optical (b) images of a reflecting phase grating. The scanned area is $5.3\times4$ $\mu$m. Cross sections of images along the diagonal are displayed at the bottom.

the surface, and the main change occurring upon a change in the clamping force is a change in the degree of bending. Thus, as the tip is scanned along the surface, the end of the fiber is in direct mechanical contact with the surface.

On account of the well-known experimental dependence of the PSTM signal on the distance between the fiber tip and the surface[2,3] the optical engagement curve a in this case can be regarded as an independent method for measuring distance. The indicated exponential dependence indeed holds right up to the point where the tip touches the surface (this point is designated as A in Fig. 3a); as the tip is brought still closer to the surface, the rate of growth of the optical signal slows down (this is especially clearly seen in the derivative of the engagement curve — Fig. 3b), since ''secondary'' factors, such as an increase in the contact area with increasing clamping force, and so on, now come into play in the formation of the signal.

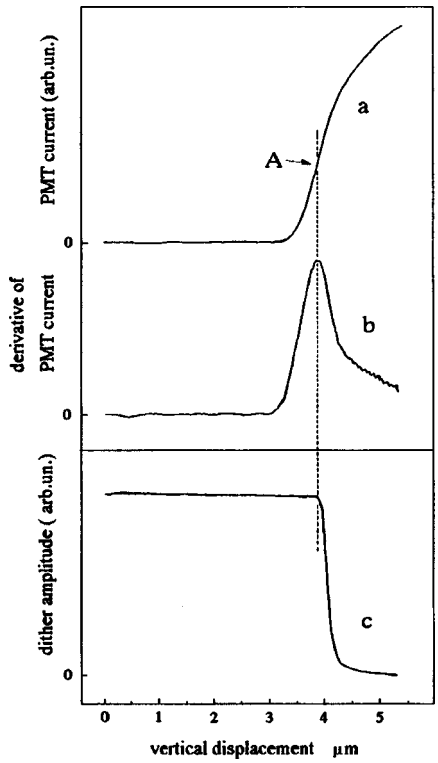


FIG. 3. Engagement curve for the optical channel (a); its derivative (b), and the engagement curve for the topographic channel (c).

During the investigations of the samples the amplitude of the oscillations was maintained equal to $\sim 0.9$ of the amplitude of free oscillations. The force acting in this case on the fiber and the sample is estimated to be $\sim 10^{-4}$–$10^{-5}$ N. This estimate is based on the stiffness $10^4$ N/m of our oscillatory unit, as follows from the elastic properties corresponding to flexural oscillations of a glass cone sharpened at the end to a radius of curvature $\sim 0.5$ $\mu$m, having an apex angle $\sim 0.1$ rad and Young's modulus $7 \times 10^{10}$ N/m$^2$ and making an angle $\sim 0.1$ rad with the surface being studied.[b)] This force is quite large, and it apparently can result in damage to samples which are too soft. At the same time, in many cases this circumstance is also an advantage of this method of microscopy, because it permits the mechanical ''scraping off'' of a thin layer of soft ''dirt'' which is always present on the sample under real conditions.

In the present letter we do not discuss in detail the dissipation mechanisms responsible for the decrease in the amplitude of the fiber vibrations used here, which are *normal* to the surface. We note only that our method can also be used in the case of a purely elastic fiber–surface interaction in the absence of any friction, for example, under conditions of high vacuum or low temperatures. In that case, even if the change in the amplitude of the oscillations is too small, scanning can be performed by utilizing the frequency channel, which is based on the change in the resonance frequency of the

piezoelectric transducer in the self-excited oscillator circuit (see above) due to the change in the purely elastic properties of the system.

In summary, a near-field microscope which operates in contact with the experimental sample and can scan quite heavy active elements (in this case — long fragments of an optical fiber) along the surface under study has been successfully realized. This makes it possible to proceed toward the practical development of FRET microscopes, which are expected to have characteristics that are unique for near-field optical microscopes. The microscope developed will also be helpful in other areas of near-field microscopy, including working at low temperatures and in a high vacuum, under conditions with insufficient free space for the classical shear-force mode, and so on.

We thank ZAO NTE, Moscow for providing the atomic-force microscope used as the basis for the near-field microscope described above. This work was supported in part by the US Department of Defense.

[a)]e-mail: sekats@isan.troitsk.ru

[1)]The formulas presented in Ref. 10 for the flexural oscillations of a cylinder can be used for rough estimates. A detailed analysis will be published later.

[1] S. K. Sekatskiĭ and V. S. Letokhov, JETP Lett. **63**, 319 (1996).
[2] D. W. Pohl and D. Courjon (Eds.), *Near Field Optics*, Kluwer, Dordrecht, 1993.
[3] R. Kopelman and W. Tan, Appl. Spectrosc. Rev. **29**, 39 (1994).
[4] P. Wu and L. Brand, Anal. Biochem. **218**, 1 (1994).
[5] D. Sarid, *Scanning Force Microscopy*, Oxford Univ. Press, London, 1991.
[6] V. N. Konopskii, S. K. Sekatskii, and V. S. Letokhov, Opt. Commun. **132**, 251 (1996).
[7] S. K. Sekatskiĭ and V. S. Letokhov, JETP Lett. **65**, 465 (1997).
[8] D. A. Lapshin, V. I. Balykin, and V. S. Letokhov, J. Mod. Opt., in press.
[9] K. V. Gogolinskiĭ, S. V. Novikov, V. N. Reshetov, and T. N. Ul'yanov, in *Structure, Phase Transformations, and Properties of Nanocrystalline Alloys* [in Russian], edited by G. G. Taluts and N. I. Noskov, Urals Branch of the Russian Academy of Sciences, Ekaterinburg, 1997, p. 102.
[10] L. D. Landau and E. M. Lifshitz, *Theory of Elasticity*, 3rd English ed., Pergamon Press, Oxford, 1986 [cited Russian original, Nauka, Moscow, 1987, Chapter 2].

Translated by M. E. Alferieff

# Spectral dependence of the excitation of the ''forbidden'' second optical harmonic in an aqueous suspension of purple membranes by femtosecond laser pulses under electronic resonance conditions

A. V. Balakin, N. I. Koroteev, A. V. Pakulev, and A. P. Shkurinov
*International Laser Center and Department of Physics, M. V. Lomonosov Moscow State University, 119899 Moscow, Russia*

D. Boucher, P. Masselin, and E. Fertein
*Laboratoire de Physico Chimie de l'Atmosphere, Universite du Littoral, 59140 Dunkerque, France*

(Submitted 8 January 1998)
Pis'ma Zh. Éksp. Teor. Fiz. **67**, No. 4, 251–255 (25 February 1998)

The spectral dependence of the efficiency of generation of the forbidden (in the electric-dipole approximation) second harmonic (FSH) and its energy on the energy of the excitation pulses is investigated experimentally in a highly disperse suspension of purple membranes containing bacteriorhodopsin (BR) under excitation by femtosecond laser pulses into the single-photon absorption band of BR. The experimental data for the case of resonance excitation attest to an interference character of the interaction of optical nonlinearities of different orders in the process leading to the formation of the FSH signal. © *1998 American Institute of Physics.* [S0021-3640(98)00504-0]

PACS numbers: 42.65.Ky, 42.70.Jk

**1**. This letter reports the results of an experimental investigation of the origin and properties of the generation of the ''forbidden'' second harmonic (FSH) in a highly disperse suspension of purple membranes containing bacteriorhodopsin (BR). Femtosecond laser pulses were used in the experiments. The center wavelength of the laser radiation could be tuned over the single-photon absorption band of BR. At the same time the frequency of the second harmonic (SH) fell into another single-photon absorption band of BR. We believe that our measurements give new important data that shed light on the mechanism of the FSH. All previous experiments on FSH generation in BR-containing suspensions have been performed under conditions such that the frequencies of the exciting pulses and of the SH pulses were fixed and lay in the transmission band of BR.

Here we shall present and analyze the frequency dependence of the efficiency of conversion into the SH and the dependence of the FSH energy on the energy of the excitation pulses for resonance excitation of the process.

**2**. The methods of nonlinear-optical diagnostics based on measurement of the frequency and temporal (on the femtosecond time scale) characteristics of coherent nonlin-

 © 1998 American Institute of Physics

ear optical processes yield unique information about the structure and dynamics of the constituent atoms and molecules of the medium.[1] Nonlinear-optical processes of lowest (second) order (such as the generation of the second optical harmonic (SH) and sum and difference frequencies (SF and DF)) are widely used for analyzing the structure and dynamics of processes occurring in molecules, crystals,[2] thin films, and on material surfaces and interfaces.[3,4] These processes, like all other nonlinear optical processes of even orders, are forbidden in the electric-dipole approximation in the bulk for isotropic media which have a center of inversion. However, despite this forbiddenness the generation of a second harmonic was recently observed in an isotropic aqueous suspension of purple membranes[5–7] under excitation by pico- and nanosecond Nd:YAG-laser pulses. Since then the nature of the origin of and the mechanism leading to the generation of the SH in an isotropic medium have been under intense investigation. Some authors attribute the appearance of this signal to incoherent hyper-Rayleigh light scattering[6] due to fluctuations of inhomogeneities of the medium. Data from other works[5,7] indicate that the FSH signal is at least partially coherent, and so there must exist one or several mechanisms of FSH generation via the macroscopic nonlinear optical susceptibilities of the medium. Indeed, since BR molecules are long and are packed in a unique manner in a membrane[8], SH generation could be due to ''nonlocal,'' i.e., magnetic-dipole and electric-quadrupole, second-order susceptibilities. Moreover, the results of our experimental investigations of FSH generation by femtosecond laser pulses[9–11] have demonstrated that it is necessary to take into account the chiral properties of BR molecules, as a result of which a suspension can be macroscopically noncentrosymmetric, which in turn removes the forbiddenness on coherent nonlinear processes via the fourth-order electric-dipole susceptibilities[12,13] (see also Ref. 14).

**3**. The object of investigation — a suspension of purple membranes containing BR molecules — was prepared by the method which we described earlier.[10] We underscore only that the average size of the membrane fragments did not exceed 50 nm. Therefore the suspension was close to being a colloidal solution. The pH of the solution was equal to 7.35. The optical density of the solution was equal to 0.12 at wavelength 570 nm. The absorption spectrum of the sample is presented in Ref. 9.

Pulsed laser radiation with wavelength tunable from 530 nm to 670 nm was used in the experiments to investigate the resonance and energy properties of the process leading to the generation of an optical field at the SH frequency. The pulse duration was equal to about 200 fs, the pulse repetition frequency was equal to 200 kHz, and the energy varied from 0 to 40 nJ/pulse. Linearly and elliptically polarized radiation was used in our experiments (in the latter case, the ratio of the semiaxes of the ellipse was 1:2). Noncollinearity of the interaction was achieved by focusing (with a lens with a focal length of 20 cm) the exciting radiation into a cell containing the experimental sample (the convergence angle of the light rays at the focal point was equal to approximately 1°). A diagram of the experimental apparatus is described in our previous paper.[9] The difference in the present experiments was that selection of the vertical component of the polarization of the SH signal was not performed at the entrance to the detection system.

**4**. We investigated the spectral dependence of the efficiency of conversion into the SH and the dependence of the FSH energy on the energy of the excitation pulse, and we analyzed the FSH spectrum. In Ref. 9 we observed that substantial differences in the polarization dependences of FSH are observed for linearly and circularly or elliptically

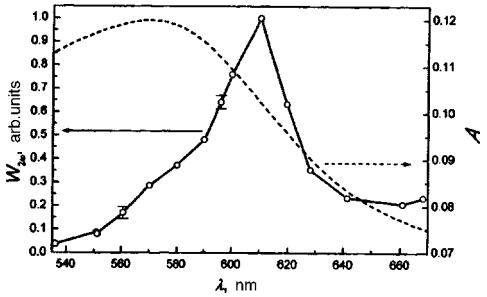


FIG. 1. FSH signal generation energy versus excitation radiation wavelength and the linear absorption spectrum of a suspension of BR-containing purple membranes. Left-hand ordinate: $W_{2\omega}$ — energy of the generated SH, ○ — experimental points; right-hand ordinate: $A$ — optical density, dashed line — absorption spectrum of the suspension, $\lambda_\omega$ — wavelength of the fundamental frequency.

polarized light. In this connection we performed experiments for two polarization states: linearly and elliptically polarized radiation at the entrance to the experimental sample.

The FSH generation efficiency versus the wavelength of the exciting radiation is displayed in Fig. 1 (elliptically polarized radiation was used to excite the sample). One can see that the dependence is of a resonance character. The curve exhibits the same characteristic trends in the case of excitation by linearly polarized radiation: The curves are similar in the region of the maximum and merge on the short- and long-wavelength edges of the spectral range presented. The maximum efficiency of conversion of the excitation radiation into the SH signal is observed for excitation wavelength $\lambda_\omega = 610$ nm. The resonance curve of FSH excitation is much narrower than the absorption band of BR, and its shape is asymmetric with respect to the extremum point: The more gently sloping ''short-wavelength wing'' drops almost to zero at $\lambda_\omega = 538$ nm, while the steeper ''long-wavelength wing'' approaches a stationary value. The ratio of the conversion efficiency at the maximum to the ''stationary'' efficiency under excitation with elliptically polarized radiation equals 5 (3.5 when the radiation at the entrance to the sample is linearly polarized). Under our experimental conditions of excitation and for the sensitivity of the system used to detect the SH radiation the FSH generation efficiency is close to zero by $\lambda_\omega = 538$ nm.

Figure 2 shows the energy of the FSH signal versus the peak power of the exciting radiation under conditions of resonance excitation of the sample ($\lambda_w = 598$ nm, $\lambda_{2\omega} = 299$ nm). Just as in our previous works on the generation of nonresonance FSH,[10,11] the dependence is more complicated, different from a simple quadratic law.

The spectra of signals at the fundamental frequency and of the FSH signal are displayed in Fig. 3. One can see from the data presented that the ratio of the width of the SH spectrum to the width of the spectrum of the radiation entering the sample equals 1.8–1.9. The same ratio ($\Delta\nu_{\mathrm{SH}}/\Delta\nu_F \leqslant 2$) holds approximately for all experimental points on the curve in Fig. 1.

**5**. In Ref. 9 it was stated and substantiated that under the conditions of resonance excitation of a suspension of BR the signal at the SH frequency contains, first and foremost, contributions due to electric-dipole nonlinearities of second-order (SF generation) and fourth-order (SH generation) in the exciting field. The energy dependence of

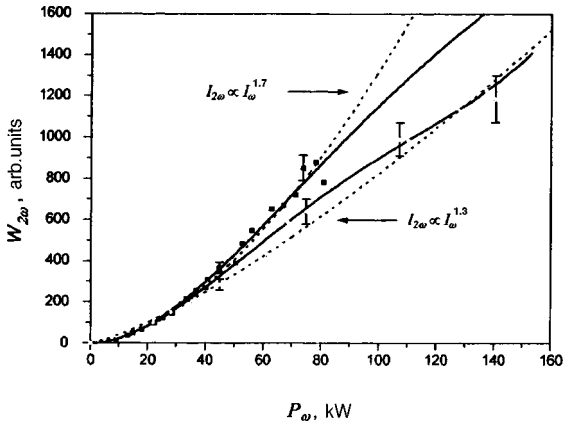


FIG. 2. Experimental points: ■ and ○ — excitation with elliptically and linearly polarized radiation. Dashed curves — fit of the experimental data by a function of the form $y=ax^b$ ($b=1.7$ and 1.3, respectively, for elliptically and linearly polarized radiation incident at the entrance to the sample). Solid curves — fit of the experimental data by a function of the form $y=a^2(x^2+2\cos(\alpha)bx^3+b^2x^4)$, where $\alpha=151°$.

FSH in Fig. 2 confirms this. It shows interference coupling of the second- and higher(fourth)-order processes. A fit of the experimental points by a power-law function $y=a\cdot x^b$ (dashed lines in Fig. 2) shows that the degree of the nonlinear FSH generation process under conditions of resonance excitation equals 1.7 for elliptically polarized wave at the entrance and 1.3 for the linearly polarized wave. Thus, one can see that the resultant signal at the SH frequency is engendered by destructive interference of second- and higher-order nonlinear processes. The experimental dependences can be satisfactorily approximated by a quartic polynomial $Y=X^2+2b\cos\alpha X^3+b^2X^4$(where $Y\approx I_{\mathrm{SH}}$, $X\approx I_F$, $b\approx|\chi^{(4)}|/|\chi^{(2)}|$, and $\alpha$ is the phase shift between the nonlinearities of second order ($\chi^{(2)}$) and fourth order ($\chi^{(4)}$) (see Refs. 10 and 11). The corresponding curves are presented in Fig. 2 (solid lines).

The existence of interference of nonlinear processes of different orders was also confirmed by the fact that the broadening of the pulse spectrum in the FSH generation

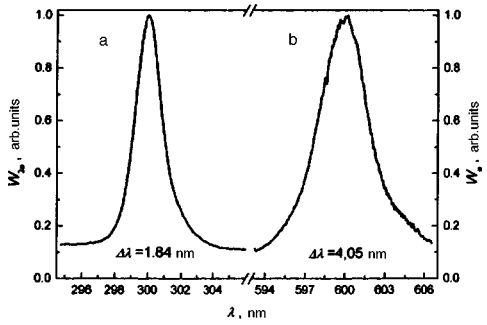


FIG. 3. Spectra of a femtosecond FSH pulse (a) and a pulse at the fundamental frequency (b). The SH signal spectrum is presented for the case when the sample is excited by elliptically polarized radiation at the fundamental frequency.

process is larger than expected for a purely quadratic process ($\Delta\nu_{SH}/\Delta\nu_F=\sqrt{2}$) and slightly less than in the fourth-order process ($\Delta\nu_{SH}/\Delta\nu_F=2$). Thus, interference is also observed at the spectral level. We note that the additional broadening occurring in the spectrum of the SH in the quadratic SH generation process during SHG of a phase-modulated pulse with negative chirp could not occur in our case, since the pump pulse was close to being spectrally limited.

The experimental facts presented above show that the frequency dependence of FSH generation efficiency (Fig. 1) can be described in terms of the destructive interference of coherent nonlinear processes of different orders, in complete agreement with the interaction picture which we proposed earlier in Refs. 10 and 11. Despite the fact that the excitation pulses used to obtain the dependence shown in Fig. 1 were comparatively low-intensity, the signal at the SH frequency still cannot be attributed to a coherent process of second order alone. This is also confirmed by the shift of the FSH conversion efficiency maximum in the long-wavelength direction relative to the absorption band maximum of BR ($\lambda=570$ nm). In the case of a second-order process this frequency dependence could have an extremum only at wavelengths corresponding to resonance at the fundamental and SH frequencies.

The spectral dependence of SHG cannot be explained by the dispersion of the coherence length of the nonlinear interaction, since the density of BR molecules in our suspension was low and the refractive index of the suspension was determined completely by that of water.

**6**. In summary, this letter reports on an investigation of the generation of the ''forbidden'' second optical harmonic in a highly disperse suspension of purple membranes containing BR molecules under excitation by femtosecond laser pulses in the visible-range absorption band of BR.

The FSH generation process under resonance excitation conditions, just as under nonresonance excitation, exhibits interference of processes which are of second and fourth order in the applied light field. Evidence for the fact that the interaction is of an interference character is provided by the measured frequency dependence of the SH generation efficiency, the dependence of the FSH energy on the excitation pulse energy, and the transformation of the width of the pump radiation spectrum.

This work was supported in part by the Russian Fund for Fundamental Research (Grants 96.02.16596, 96.03.34067). The Laboratoire de Phyico Chimie de l'Atmosphere is a member of the Center d'Etude et de Recherche des Lasers et Application. A.V.B., A.V.P. and A.P.S. thank Universite du Littoral, Dunkerque for making available invited positions for the period during which the experiments were performed. A.V.B. also acknowledges the Samsung Electronics Company for providing partial support for participation in the experiment.

[1] N. I. Koroteev, Vestn. Mosk. Univ. Fiz. Astron. No. 6, 6 (1996).
[2] Y. R. Shen, *The Principles of Nonlinear Optics*, Wiley, New York, 1984 [Russian translation, Nauka, Moscow, 1989].
[3] G. A. Reider and T. F. Heins, ''Second-order nonlinear optical effects at surfaces: recent advances,'' in *Photonic Probes of Surfaces*, edited by P. Halevi, Elsevier Science, Amsterdam 1995, p. 415.
[4] S. A. Akhmanov, N. I. Koroteev, and I. L. Shumay, in *Nonlinear Optical Diagnostics of Laser-Excited Semiconductor Surfaces*, edited by V. S. Letokhov, C. V. Shank, Y. R. Shen, and H. Walther, Harwood Academic Publishers, London, 1989.

[5] Q. Song, C. Wan, and C. K. Johnson, J. Phys. Chem. **98**, 1999 (1994).
[6] P. K. Schmidt and G. W. Rayfield, Appl. Opt. **33**, 4286 (1994).
[7] P. Allcock, D. L. Andews, S. R. Meech, and A. J. Wigman, Phys. Rev. A **53**, 2788 (1996).
[8] T. A. Ceska and R. Henderson, J. Mol. Biol. **213**, 539 (1990).
[9] A. V. Balakin, D. Boucher, N. I. Koroteev *et al.*, Zh. Éksp. Teor. Fiz. **112**, 97 (1997). [JETP **85**, 52 (1997)].
[10] A. V. Balakin, D. Boucher, E. Fertein *et al.*, Opt. Commun. **141**, 343 (1997).
[11] A. V. Balakin, D. Boucher, N. I. Koroteev *et al.*, JETP Lett. **64**, 718 (1996).
[12] N. I. Koroteev, in *Frontiers in Nonlinear Optics*, The Sergei Akhmanov Memorial Volume, edited by H. Walther, N. Koroteev, and M. Sculy, Inst. of Phys. Publishing, Bristol 1993, p. 228.
[13] N. I. Koroteev, Zh. Éksp. Teor. Fiz. **106,** 1260 (1994) [JETP **79**, 681 (1994)].
[14] P. Allcock and D. L. Andrews, J. Phys. B.: At. Mol. Opt. Phys. **30**, 3731 (1997).

Translated by M. E. Alferieff

# Spontaneous far-IR emission accompanying transitions of charge carriers between levels of quantum dots

L. E. Vorob'ev,[a] D. A. Firsov, and V. A. Shalygin
*St. Petersburg State Technical University, 195251 St. Petersburg, Russia*

V. N. Tulupenko
*Donbass State Mechanical Engineering Academy, 343913 Kramatorsk, Ukraine*

Yu. M. Shernyakov, N. N. Ledentsov, V. M. Ustinov, and Zh. I. Alferov
*A. F. Ioffe Physicotechnical Institute, Russian Academy of Sciences, 194021 St. Petersburg, Russia*

(Submitted 15 January 1998)
Pis'ma Zh. Éksp. Teor. Fiz. **67**, No. 4, 256–260 (25 February 1998)

The spontaneous emission of far-infrared radiation ($\lambda \cong 10$–$20$ $\mu$m) from diode structures with vertically coupled InGaAs/AlGaAs quantum dots is observed. This emission is due both to transitions of holes and electrons between size-quantization levels in quantum dots and to transitions from the continuum to a level in a quantum dot. It is observed only when accompanied by lasing at short wavelengths ($\lambda \cong 0.94$ $\mu$m) and, like the short-wavelength emission, it exhibits a current threshold. The spontaneous emission of long-wavelength radiation is also observed in InGaAs/GaAs quantum-well laser structures. This radiation is approximately an order of magnitude weaker than that from quantum-dot structures, and it has no current threshold. © *1998 American Institute of Physics.* [S0021-3640(98)00604-5]

PACS numbers: 85.30.Vw, 73.20.Dx, 78.30.Fs

## INTRODUCTION

Intersubband optical transitions of charge carriers in quantum wells have been investigated in detail, and these investigations have already led to the development of IR detectors and modulators.[1] Among the latest achievements in this direction we call attention to the development of a quantum cascade laser,[2] based on a modification of an idea from Ref. 3, and a ''fountain'' laser.[4] The study of transitions of charge carriers between levels in quantum dots (QDs) opens up new prospects in the development of far-IR range ($\lambda > 10$ $\mu$m) devices. However, only light absorption accompanying transitions between localized states of electrons in QDs and the continuous spectrum as well as transitions of holes between different levels in a QD have been investigated thus far.[5]

In the present work we observed spontaneous emission accompanying both transitions of electrons from the continuum to levels of QDs and interlevel transitions of holes in quantum dots. A necessary condition for observing this physical process is the simultaneous generation of radiation in QDs via the ground states of localized electrons and

 © 1998 American Institute of Physics

holes ($h\nu$ close to $\varepsilon_g$), which ensures depopulation of the lower (ground) electron and hole levels in QDs under the conditions of high levels of current injection of electron–hole pairs in a QD heterolaser. The observation of spontaneous emission can be interpreted as the first step in the development of a far-IR laser operating on interlevel transitions of charge carriers in QDs.

### EXPERIMENTAL SAMPLES AND PROCEDURE

The samples consisted of laser structures with vertically-coupled QDs, as described in Ref. 6. The active region of such a laser is a $Al_{0.15}Ga_{0.85}As$ laser with self-organized $In_{0.5}Ga_{0.5}As$ quantum dots. There are 10 layers. An $Al_{0.15}Ga_{0.85}As$ layer is 5 nm thick. This thickness is comparable to the size of quantum dots in a direction perpendicular to the layers. Thus, the QDs are tunneling-coupled in the vertical direction. Stimulated emission corresponded to the near-IR range: The lasing wavelength was about 0.94 $\mu$m (at 300 K). A FD8-K silicon photodiode was used to detect this radiation. Radiation was observed in the pulsed regime, and the duration of the current pulses was equal to 200 ns. For a cavity-mirror separation of approximately 1100 $\mu$m the threshold current density $j_{th}$ at $T=300$ K was equal to approximately 290 A/cm$^2$ (the threshold current $I_{th}=0.6$ A). Dielectric mirrors were not deposited.

Ge⟨Cu⟩ and Si⟨B⟩ photodetectors with sensitivity in the range $\lambda=5-29$ $\mu$m at close to liquid-helium temperature were used to observe far-IR emission from the same structures. InSb and Ge filters were installed at the entrances of the photodetectors in order to cut off the near-IR radiation ($\lambda\cong 0.94$ $\mu$m). $BaF_2$, NaCl, and KBr filters were used to determine the spectral composition of the far-IR emission more accurately. The far-IR emission investigations were performed at $T=30$ K (likewise in the pulsed mode).

The spontaneous far-IR emission from $In_{0.2}Ga_{0.8}As/GaAs$ laser structures with 7 nm wide quantum wells (QWs) was investigated in parallel. These structures were constructed for the purpose of generating stimulated near-IR emission.

## RESULTS AND DISCUSSION

Figure 1a shows the signals from the photodetectors for stimulated near-IR and spontaneous far-IR emission from a QD laser structure. Using a system of filters, it was established that the far-IR emission is concentrated in the range 10–20 $\mu$m. We note that the dependence of the spontaneous far-IR emission intensity on the laser current is of a threshold character, the current threshold being close to the current threshold $I_{th}$ for stimulated near-IR emission, which was equal to 0.33 A at low temperatures (approximately half the room-temperature threshold). Thus far-IR emission can be detected only simultaneously with generation of near-IR emission ($\lambda\cong 0.94$ $\mu$m). An entire series of similar samples with QD-laser structures was investigated. In the structures where there was no stimulated near-IR emission spontaneous far-IR emission also was not observed.

Next, similar investigations were performed on $In_{0.2}Ga_{0.8}As/GaAs$ quantum-well laser structures (Fig. 1b). The threshold current for stimulated near-IR emission for QW structures was equal to approximately 0.25 A. We also observed spontaneous far-IR emission in these structures. The far-IR emission was approximately an order of magnitude weaker than in QD structures, and in contrast to the latter structures it was not of a threshold character.

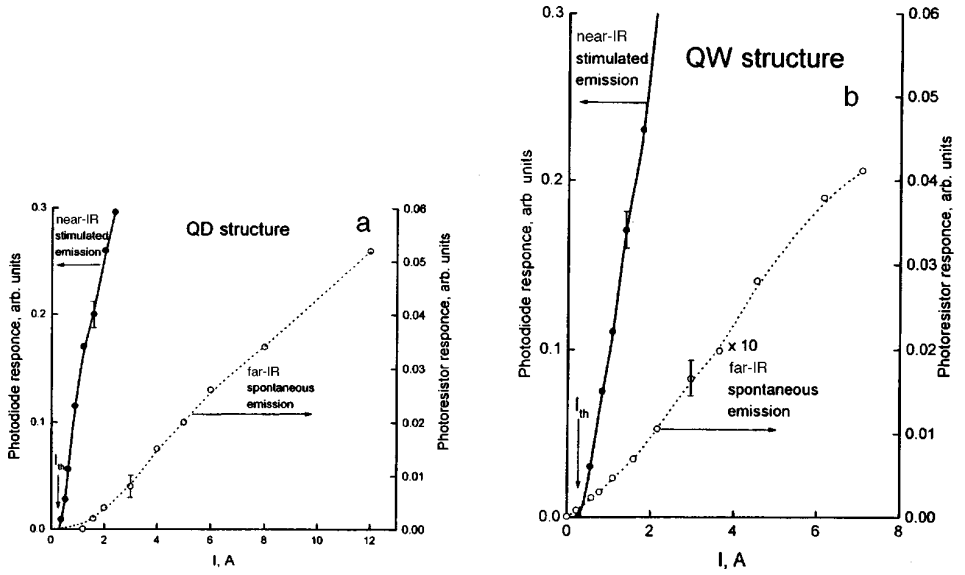


FIG. 1. Spontaneous far-IR emission ($\lambda \cong 10$–$20$ $\mu$m) and stimulated near-IR emission ($\lambda = 0.94$ $\mu$m) intensity versus the current through the structure. Temperature $T = 30$ K. The near-IR emission detected with a Si photodiode, the far-IR emission was detected with Ge⟨Cu⟩ or S⟨B⟩ photoresistors. a — For a structure with InGaAs/AlGaAs quantum dots ($I_{\text{th}}$ is the threshold current for both near- and far-IR emission). b — For an InGaAs/GaAs quantum-well structure ($I_{\text{th}}$ is the threshold current for near-IR emission; there is no threshold for far-IR emission).

We shall now give a qualitative explanation of the observed phenomena. We discuss first the possibility of spontaneous far-IR emission for QD laser structures. Let us assume the level structure in the InGaAs/AlGaAs quantum dots studied is similar to that calculated in Ref. 6 for pyramidal InAs/GaAs quantum dots with 10–12 nm base. Such quantum dots have one electronic level $|000\rangle$ (our structures can have two electronic levels) and four hole levels $|000\rangle$, $|100\rangle$, $|001\rangle$, and $|110\rangle$ (see Fig. 2a). When electrons (holes) are injected into the AlGaAs layer they are trapped in a state in the wetting layer within a time of the order of several picoseconds,[8,9] after which a transition occurs into an electronic (hole) level in the quantum dot. Holes in QDs can also undergo interlevel transitions of the type $|100\rangle \rightarrow |000\rangle$, $|001\rangle \rightarrow |000\rangle$, and $|110\rangle \rightarrow |000\rangle$. Transitions from upper to lower states can be accompanied by emission of phonons[8–10] or a 10–20 $\mu$m photon or (at high charge-carrier densities) they can due to Auger-type processes.[11] According to Ref. 8, the transition time between the excited and ground states of holes is approximately 40 ps (tens of picoseconds[9]).

In Ref. 5 absorption peaks near 115 meV for transitions between hole levels in a InAs/GaAs QD and near 190 meV for electron transitions from a QD level into the continuum were observed with electron–hole pair excitation by interband light. Saturation of light absorption by holes was observed for exciting light intensity $\sim 100$ W/cm$^2$. This signifies that the hole ground levels in the QDs are completely filled. If one assumes that the processes occurring in a system of coupled InGaAs/AlGaAs QDs are similar, then one should expect that the ground levels in InGaAs/AlGaAs QDs are filled at the same light intensity. For threshold currents $I_{\text{th}} \cong 0.3$ A ($j_{\text{th}} \cong 140$ A/cm$^2$) approximately

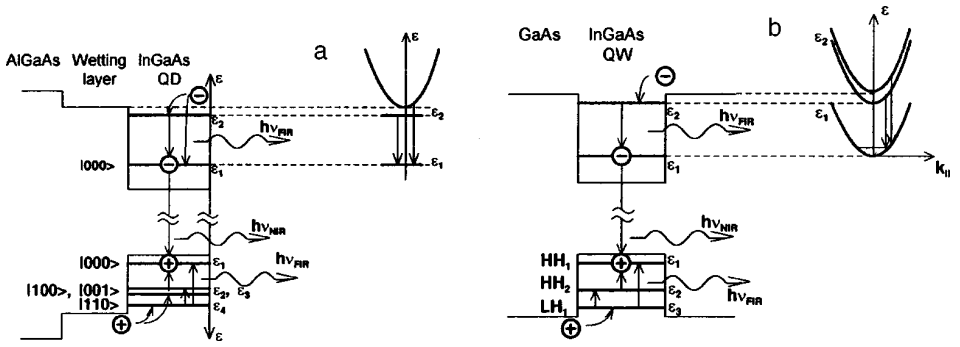


FIG. 2. a — Scheme of optical electron and hole transitions, resulting in spontaneous far-IR emission, between size-quantization levels in InGaAs/AlGaAs quantum dots and between states in an AlGaAs layer and levels in quantum dots. Depopulation of unexcited (ground) electron and hole levels occurs as a result of induced interband near-IR emission. b — Same, but for InGaAs/GaAs quantum-well laser structures. The energies of the levels are measured from the well bottom. Electronic levels: $\varepsilon_1=48$ meV, $\varepsilon_2=156$ meV; well depth for electrons 163 meV. Hole levels: $\varepsilon_1=12$ meV, $\varepsilon_2=45$ meV, and $\varepsilon_3=79$ meV; well depth for heavy holes 80 meV.

twice as many electron–hole pairs are produced as by light with intensity $J^{\nu}\cong 100$ W/cm$^2$. The hole (electron) ground states in the QDs are filled and optical transitions into them from the excited states in QDs or states in QWs (Fig. 2a) are impossible.

Stimulated near-IR emission occurs at pump currents above $I_{\text{th}}$, and the corresponding interband transitions partially depopulate the electron and hole ground states in QDs. Electron and hole transitions into them from excited states engender spontaneous far-IR emission. The intensity of this emission is proportional to the number $N_{\text{ex}}$ of charge carriers in excited states and the probability that the lower states are empty. The number $N_{\text{ex}}$ is a linear function of the current, while the probability that the lower states are emptied increases with the stimulated near-IR emission intensity.

As the pump current increases, increasingly more quantum dots of different sizes are brought into the near-IR emission process. This is indicated, for example, by the relatively low differential quantum efficiency $\eta^{\nu}=dJ^{\nu}_{NIR}/dI$ at low temperatures (as $T$ increases from 30 K to 300 K, $\eta^{\nu}$ increases). For the reasons indicated the far-IR emission intensity $J^{\nu}_{FIR}$ can grow in a faster-than-linear manner, as experiment confirms. According to our data, $J^{\nu}_{FIR}\propto I^2$ for $I>I_{\text{th}}$ (see Fig. 1a). As the current through the structure increases further, the function $J^{\nu}_{FIR}(I)$ gradually goes over to a linear dependence, possibly as a result of the transfer of holes (electrons) from the upper states by the powerful stimulated emission and an increase in the role of Auger processes.[11]

Let us now discuss the observed characteristics of spontaneous far-IR emission for QW laser structures. According to the calculations, a $In_{0.2}Ga_{0.8}As/GaAs$ QW with well width $L_W=7$ nm contains two size-quantization electron levels (Fig. 2b) the energy splitting between which is $\varepsilon_2-\varepsilon_1=108$ meV. For holes there are three levels: $\varepsilon_1=12$ meV, $\varepsilon_2=45$ meV (heavy-hole subbands $HH_1$ and $HH_2$), and $\varepsilon_3=79$ meV (light-hole subbands $LH_1$). Transitions between electron and hole size-quantization subbands in QWs can also contribute to emission in the range $\lambda=10$–$20$ $\mu$m. The number of charge carriers in excited states (upper subbands) is proportional to the current through the

structure. The bottom (ground) subbands always contain unfilled states into which holes (or electrons) are transferred (Fig. 2a). For this reason, the far-IR emission intensity is approximately proportional to the current $J_{FIR}^{\nu} \propto I$ and has no threshold, as is observed experimentally (Fig. 1b). Moreover, it should be noted that, according to data obtained by different authors, the lifetime of charge carriers in excited states in a QW ranges approximately from a fraction of a picosecond to several picoseconds, which is more than an order of magnitude shorter than for QDs. For this reason, the far-IR emission intensity for structures with QWs should be less than for structures with QDs. Indeed, it has been found experimentally that far-IR emission is approximately an order of magnitude weaker for QWs than for QDs.

In summary, we have observed spontaneous emission due to transitions of charge carriers between levels in quantum dots under conditions of interband short-wavelength lasing in laser QD structures. Far-IR emission from QD structures is approximately an order of magnitude stronger and exhibits a more pronounced threshold character than the analogous emission from QW structures. Comparing the emission intensity for both cases shows that the charge-carrier lifetime in QDs is at least an order of magnitude longer than in QWs. This gives hope for obtaining a population inversion of holes or electrons under near-IR interband radiation generation conditions and for producing on the basis of QD structures new, more efficient, light-emitting far-IR devices, specifically, a far-IR laser operating on interlevel transitions of charge carriers in QDs.

This work was supported in part by the Russian Fund for Fundamental Research, Grant 96-02-17404; INTAS-REBR, Grant 00615i96; the Ministry of Science and Technology under the program ''Physics of Solid-State Nanostructures,'' Grant 96-1029; and, the Federal Target Program ''Integration,'' Project No. 75.

[a)]e-mail: LVor@phsc2.stu.neva.ru

[1] E. Rosencher and B. Levine (eds.), *Intersubband Transitions in Quantum Wells*, NATO ASI Series, Ser. B, Physics Vol. 288, Plenum Press, New York, 1992.
[2] J. Faist, F. Capasso, D. L. Sivco *et al.*, Science **264**, 553 (1994).
[3] R. F. Kazarinov and R. A. Suris, Fiz. Tekh. Poluprovodn. **5**, 797 (1971); **6**, 148 (1972) [Sov. Phys. Semicond. **5**, 707 (1971); **6**, 120 (1972)].
[4] O. Gauthier-Lafaye, S. Sauvage, P. Boucaud *et al.*, Appl. Phys. Lett. **70**, 3197 (1997); in *Proceedings of International Symposium ''Nanostructures: Physics and Technology,''* St. Petersburg, 1997, p. 567.
[5] S. Sauvage, P. Boucaud, F. H. Julien *et al.*, Appl. Phys. Lett. **71**, 2785 (1997).
[6] M. V. Maximov, Yu. M. Shernyakov, N. N. Ledentsov *et al.*, in *Proceedings of International Symposium on ''Nanostructures: Physics and Technology,''* St. Petersburg, 1997, p. 202.
[7] M. Grundmann, O. Stier, and D. Bimberg, Phys. Rev. B **52**, 11969 (1995).
[8] R. Heitz, M. Veit, N. N. Ledentsov *et al.*, Phys. Rev. B **56**, 10435 (1997).
[9] N. N. Ledentsov, in *The Physics of Semiconductors*, edited by M. Scheffler and R. Zimmermann, World Scientific, Singapore, V.**1**, 1996, p. 19.
[10] M. J. Steer, D. J. Mowbray, M. S. Skolnick *et al.*, in *The Physics of Semiconductors*, edited by M. Scheffler and R. Zimmermann, World Scientific, Singapore, V.**2**, 1996, p. 1389.
[11] J. H. H. Sandmann, G. von Plessen, J. Feldman *et al.*, in *Program and Abstracts of 10th International Conference on Nonequilibrium Carrier Dynamics in Semiconductors*, Berlin, Report MoD3 (1997).

Translated by M. E. Alferieff

# On phase-modulational bifurcation during passive mode locking in lasers

A. K. Komarov, K. P. Komarov,[a)] and A. S. Kuch'yanov
*Institute of Automation and Electrometry, Siberian Branch of the Russian Academy of Sciences, 630090 Novosibirsk, Russia*

(Submitted 9 January 1998)
Pis'ma Zh. Éksp. Teor. Fiz. **67**, No. 4, 261–264 (25 February 1998)

We have found that phase-modulation instability of a single pulse due to nonlinearity of the refractive index of an in-cavity medium can cause the pulse to break up into several stable identical pulses of smaller amplitude. We show that if the refractive-index nonlinearity is greater than a critical value, then stabilization of the regime with several stationary pulses does not occur, and pulse multiplication accompanied by chaotic variation of the intensity continues until the cavity is completely filled with radiation. © *1998 American Institute of Physics.* [S0021-3640(98)00704-X]

PACS numbers: 42.60.Mi, 42.60.Fc

**1**. Phase modulation of generated pulses plays an important role in the formation of subpicosecond and femtosecond laser pulses with passive mode locking.[1] Phase-modulation pulse instability, which leads to a change in the lasing regimes established at the completion of the transient process, appears both in conventional systems using the nonlinear losses of saturable absorbers and in lasers whose nonlinear losses are due to an in-cavity Kerr lens.[2] A similar instability arises in fiber communication lines with periodic amplification cascades. The field evolution in these systems is described by a nonlinear Schrödinger equation[3] with complex parameters. In the case of nonlinearities of a special form, this equation becomes the Ginzburg–Landau equation employed for describing hydrodynamic instabilities,[4] which are the analog of phase-modulation instability in optics.

In the present letter we report the results of investigations of the change induced in the in-cavity radiation states by a phase-modulation instability due to a change in the parameters of the in-cavity nonlinear dispersive medium. The characteristic features which we found for the transition from the one-soliton lasing regime described by a nonlinear Schrödinger equation with complex parameters to a multisoliton regime and then to a chaotic regime can be manifested in a large class of physical systems.

**2.** In the model of a distributed in-cavity medium, the equation describing the evolution of in-cavity radiation in dimensionless variables in a coordinate system moving with the pulse has the form[5]

 © 1998 American Institute of Physics

$$\frac{\partial}{\partial t}E=(1+id)\frac{\partial^2}{\partial z^2}E+\frac{1}{2}\left(\frac{1+\alpha}{1+b\int|E|^2dz}-1-\frac{p}{1+|E|^2}+iq|E|^2\right)E, \quad (1)$$

where $E(z,t)$ is the slow amplitude of the field, $t$ is the time variable expressed in units of the decay time of the field in an empty cavity, $z$ is the coordinate expressed in units of the dispersion length (geometric-mean of the reciprocal of the decay time of the field in an empty cavity and the frequency dispersion of the imaginary part of the permittivity), $d$ is the ratio of the real and imaginary parts of the frequency dispersion of the in-cavity medium. The first term in parentheses describes the saturable gain (the saturation is determined by the total energy of the in-cavity radiation; $\alpha$ is the relative pump excess above threshold; $b$ is the ratio of the saturation intensities of nonlinear losses and amplification divided by the dimensionless cavity length), the second term accounts for the linear cavity losses, and the third term describes the nonlinear losses. The last term accounts for the refractive-index nonlinearity.

In the case $d=0$, $q=0$ (no phase modulation of ultrashort pulses), the evolution of the system always culminates in a stationary state ($\dot{E}=0$), irrespective of the initial conditions.[5] The same thing also happens with $d\neq 0$ if the radiation intensity is sufficiently low, $|E|^2\ll 1$, and the complex dispersion and nonlinearity satisfy the condition $d=q/p$ (in this case the phase-modulation mechanisms due to refractive-index nonlinearity and dispersion compensate one another). When the threshold locking conditions are satisfied, a regime with a single stationary pulse is established.

**3**. Let us investigate the role played by phase modulation of in-cavity radiation in the realization of states of different types established after transient evolution. Let the phase modulation be due to refractive-index nonlinearity only, $d=0$. To solve the problem of the evolution of a light wave propagating in the nonlinear dispersive in-cavity medium we integrated Eq. (1) numerically with different values of the parameters of the problem.

For sufficiently small pump excess above threshold, $|E|^2\ll 1$, the change in the nonlinear losses is determined by the expression

$$\delta p\approx p|E|^2. \quad (2)$$

As our numerical calculations showed, in this case, for not too large refractive-index nonlinearity, $0\leqslant|q|<3p$, a regime with a single stationary pulses is realized after transient evolution. For $|q|>3p$ this regime becomes unstable and a different lasing regime is established. The instability is manifested as follows. New pulses appear on the far wings of the initial pulse. Pulse multiplication arises and continues until radiation completely fills the cavity. The change in the cavity field is chaotic. In addition, since the total energy of the in-cavity radiation is limited, as the pulses multiply, the intensity of each pulse decreases and the nonlinear process of infinite chaotic fragmentation of pulses slows down.

The instability mechanism is determined by the following circumstance. On account of the refractive-index nonlinearity on the pulse wings the carrier frequency of the radiation is detuned from the center of the spectral gain band of the in-cavity active medium. As a result, the removal of the population inversion and, correspondingly, the amplification of the pulse formed become less efficient. The critical point is $|q|=3p$, where the

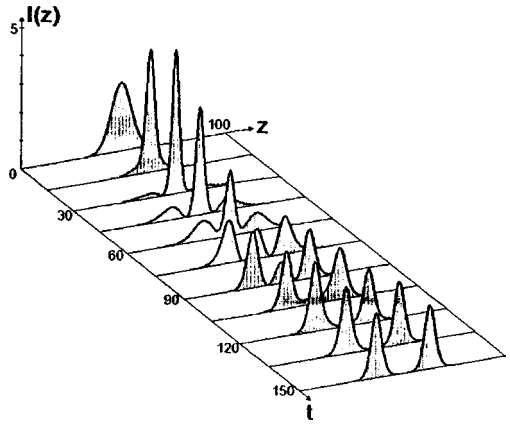


FIG. 1. Transient process with $\alpha=4$, $b=0.1$, $p=0.3$, and $q=0.3$. The initial pulse is Gaussian.

amplification gain due to loss nonlinearity equals the loss due to the detuning of the carrier frequency as a result of the refractive-index nonlinearity. In consequence, for $|q|>3p$ the gain outside the volume of the phase-modulated pulse is positive, as a result of which new pulses with no appreciable initial phase modulation appear in the generation.

**4**. In all real systems the linear intensity dependence (2) of the change in losses holds only for sufficiently weak fields. For strong fields the change in the nonlinear losses is determined by the expression

$$\delta p=\frac{-p}{1+|E|^2}+p=\frac{p}{1+|E|^2}|E|^2=p_{\text{eff}}|E|^2. \tag{3}$$

As the numerical calculations showed, for $|q|>3p$ pulse multiplication arises once again and the process terminates when the time-varying radiation fills completely fills the laser cavity. However, the situation changes fundamentally in the region $3p>|q|>3p_{\text{eff}}$. For $|q|>3p_{\text{eff}}$ the initial pulse starts to break up. Since the total energy of the radiation is limited, the intensity of each newly formed pulse decreases, $p_{\text{eff}}$ correspondingly increases, and finally the break-up process stops when $|q|<3p_{\text{eff}}$. Figure 1 demonstrates the phase-modulation instability of single pulse and the appearance of a regime with two stable identical stationary pulses after the transient evolution. As the numerical calculations show, in the established state the total gain, including losses, outside the volume of the pulses is negative. As the refractive-index nonlinearity $|q|$ increases, stable regimes with three stationary pulses ($|q|=0.4$), four pulses ($|q|=0.5$), and so on appear in succession (the other parameters of the system were the same as those given in the figure caption). For supercritical nonlinearity, $|q|>0.9$, a generation regime in which the time-varying radiation completely fills the cavity is established.

We also investigated the dependence of the established state on the in-cavity radiation energy. As the laser pump $\alpha$ increases, the in-cavity intensity increases, $p_{\text{eff}}$ decreases, and correspondingly the number of stable stationary pulses in the established generation regime increases. Thus, for other parameters of the system equal to the values

indicated in the figure, a regime with two stationary pulses obtains for $\alpha = 2.5$, three stationary pulses for $\alpha = 5$, four stationary pulses for $\alpha = 7.4$, and so on.

**5**. So, phase-modulation instability due to refractive-index nonlinearity results in a change in the generation regime that is established after transient evolution. This change is followed by an increase in the number of stable stationary pulses in the established regime. If the nonlinearity exceeds the critical level, then phase-modulation instability leads to a generation regime in which the time-varying radiation completely fills the laser cavity.

It should be noted that in the system studied the transition to the single-pulse regime and the pulse break-up mechanism are due to the following circumstance. In the first case the eigenvalues obtained by solving the eigenfunction and eigenvalue problem for Eq. (1) with a prescribed potential determined by the distribution $E(z)$ at a given time always satisfy the condition that the real part of the eigenvalue is maximum for the fundamental state. Transient evolution is a transition into this state, characterized by the maximum gain, from a superposition of any other states (see Ref. 5). Pulse break-up arises when this condition, which in the case of a real potential $(q = 0)$ follows from the oscillatory quantum-mechanical theorem,[6] is not satisfied on account of the complexity of the nonlinearity.

We acknowledge E. A. Kuznetsov for his interest in this work. These investigations were supported by the Russian Fund for Fundamental Research (Grant 96-02-19367) and the State Science and Technology Program ''Laser Physics'' (Grant 3.20).

[a)]e-mail: komarov@iae.nsk.su

[1] L. Kramer, E. A. Kuznetsov, S. Popp, and S. K. Turitsyn, JETP Lett. **61**, 904 (1995).
[2] H. A. Haus, J. P. Fujimoto, and E. P. Ippen, J. Opt. Soc. Am. B **8**, 2068 (1991).
[3] V. E. Zakharov, in *Handbook of Plasma Physics*, edited by A. Galeev and Sudan, Elsevier, Amsterdam, Vol. 3, 1984, p. 81.
[4] E. Kaplan, E. Kuznetsov, and V. Steinberg, Phys. Rev. E **50**, 3712 (1994).
[5] K. P. Komarov, Opt. Commun. **54**, 233 (1985).
[6] L. D. Landau and E. M. Lifshitz, *Quantum Mechanics: Non-Relativistic Theory*, 3rd edition, Pergamon Press, Oxford, 1977 [Russian original, Nauka, Moscow, 1974].

Translated by M. E. Alferieff

# One-dimensional localization in porous $a$-$Si_{1-c}Mn_c$

A. I. Yakimov,[a] A. V. Dvurechenskiĭ, V. A. Dravin, and Yu. Yu. Proskuryakov

*Institute of Semiconductor Physics, Siberian Branch of the Russian Academy of Sciences, 630090 Novosibirsk, Russia*

(Submitted 6 January 1998)
Pis'ma Zh. Éksp. Teor. Fiz. **67**, No. 4, 265–269 (25 February 1998)

The temperature dependence of the conductance of porous silicon doped with manganese up to densities corresponding to the metallic side of the Anderson transition is investigated. It is found that in the temperature range below $T=40$–$60$ K the conductance decreases with $T$ as $G(T)\propto T^{-1/3}$. This behavior corresponds to one-dimensional electron localization in silicon wires under conditions of inelastic electron–electron collisions with a small energy transfer. © *1998 American Institute of Physics.* [S0021-3640(98)00804-4]

PACS numbers: 72.80.Ng, 72.15.Rn

According to classical ideas based on the Boltzmann equation, the conductance of metals increases with decreasing temperature. The situation changes when disorder is present in the system. In this case the wave properties of the electrons give rise at low temperatures to quantum corrections that decrease the conductance compared to the Boltzmann value.[1] The first correction is due to the dynamic effect of the electron–electron interaction. The second correction is due to electron localization as a result of the interference of the scattered waves. The theory of these phenomena is called the theory of weak localization. For a three-dimensional bulk sample the relative magnitude of the corrections is of the order of $(k_F l)^{-2}$, where $k_F$ is the wave vector at the Fermi surface and $l$ is the mean free path. For this reason the quantum effects are largest near the Anderson transition, where $k_F l\sim 1$. Comparing the interference correction to the conductance to the correction due to the interaction shows that in a three-dimensional (3D) system the effect due to the electron–electron interaction predominates, for a 2D system both corrections are of the same order of magnitude, and in a 1D metal the interference correction predominates.[2]

Quantum corrections have been most actively investigated in 2D and 3D systems (see the review in Ref. 1). A necessary condition for observing 1D localization is $L_\varphi > b$, where $L_\varphi$ is the phase coherence length and $b$ is the diameter of a wire. The one-dimensional wires have been produced by means of either a complicated electron lithography technique[3–5] or extrusion.[6] The minimum diameter obtainable by such methods is $\sim 100$ nm and the relative correction to the resistance does not exceed 1% at $T=4.2$ K. The value of $b$ can be decreased to 50 nm by exotic methods, such as growing a heterojunction on the face of a superlattice.[7] In our previous works we showed that under certain conditions electrochemical etching of amorphous silicon ($a$-Si) in a solution

 © 1998 American Institute of Physics

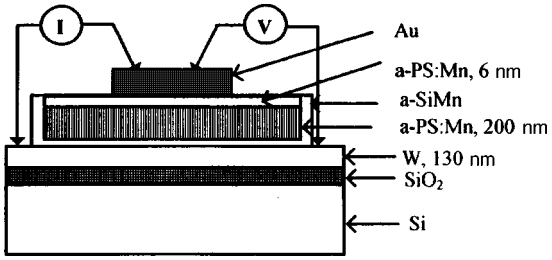


FIG. 1. Diagram of the experimental structure and the measurement scheme.

of hydrofluoric acid produces conducting regions of silicon 5–8 nm in diameter, which lie perpendicular to the surface and are surrounded by depletion regions and pores. The study of charge transfer on the insulator side of the Anderson transition showed that the conductance in porous *a*-Si doped with manganese up to concentrations $c=4\%$ and 7% is determined by electron hops along quasi-one-dimensional trajectories bounded by the walls of pores.[8] In the present letter we report the results of an investigation of porous $a\text{-}Si_{1-c}Mn_c$ for impurity concentrations corresponding to metallic conduction ($c \geqslant 14\%$). It was found that 1D electron localization is observed in such structures at temperatures below 40–60 K. The interference correction to the conductance increases with Mn concentration and reaches values $>6\%$ at $T=4.2$ K for $c=22\%$.

A cross section of the structure employed for the measurements is presented in Fig. 1. A tungsten film 130 nm thick, separated from the silicon substrate by a $SiO_2$ dielectric layer, served as the bottom electrical contact. A film of amorphous silicon 250 nm thick was deposited on the tungsten in ultrahigh vacuum by molecular-beam epitaxy. The substrate temperature due to heating from the electron-beam evaporator did not exceed 50 °C, The *a*-Si was doped by implantation of $Mn^+$ ions. The ion current density was equal to 3.3 $\mu$A/cm$^2$ and the irradiation dose was $\sim 10^{17}$ cm$^{-2}$. A uniform impurity distribution over the entire 250 nm thickness was achieved by varying the energy of the ions in the range 20–260 keV. Investigations of the conductance of $a\text{-}Si_{1-c}Mn_c$ layers prepared by this method showed that a transition of the system into a metallic state (Anderson transition) occurs for $c \geqslant 14\%$.[9,10] The next step was electrolytic etching in a solution 42% $HF:H_2O:C_2H_7OH$ (1:1:2) for the purpose of producing 1D silicon wires. In the process pores oriented predominantly in a direction perpendicular to the surface are formed in the material. The regions of silicon near the surface of the pores are carrier-depleted and, as a result, 1D conducting channels 5–8 nm in diameter are formed. A high-resolution electron microscope image of a cross section of porous *a*-Si has been published in Ref. 8. The porous layer in the experimental structures consisted of two parts (Fig. 1): a thin ($\sim 6$ nm) contact layer with a porosity of about 30% on top, and the main, approximately 200 nm thick, bottom layer with a porosity of 50–60%. The bilayer nature of the structure was achieved by varying the anodic-etching current from 2 to 15 $\mu$A/cm$^2$ in the course of electrolysis. The fabrication of the structure was completed by depositing a $5\times 10^{-3}$ cm gold pad on top. The conductance was measured by the four-probe ac method. The current strength was equal to 0.1–1.0 $\mu$A, the frequency of the current was equal to 0.1–4 kHz, and the voltage drop across the samples did not exceed 1 $\mu$V. Under such conditions the resistance of the samples did not depend on the measurement method.

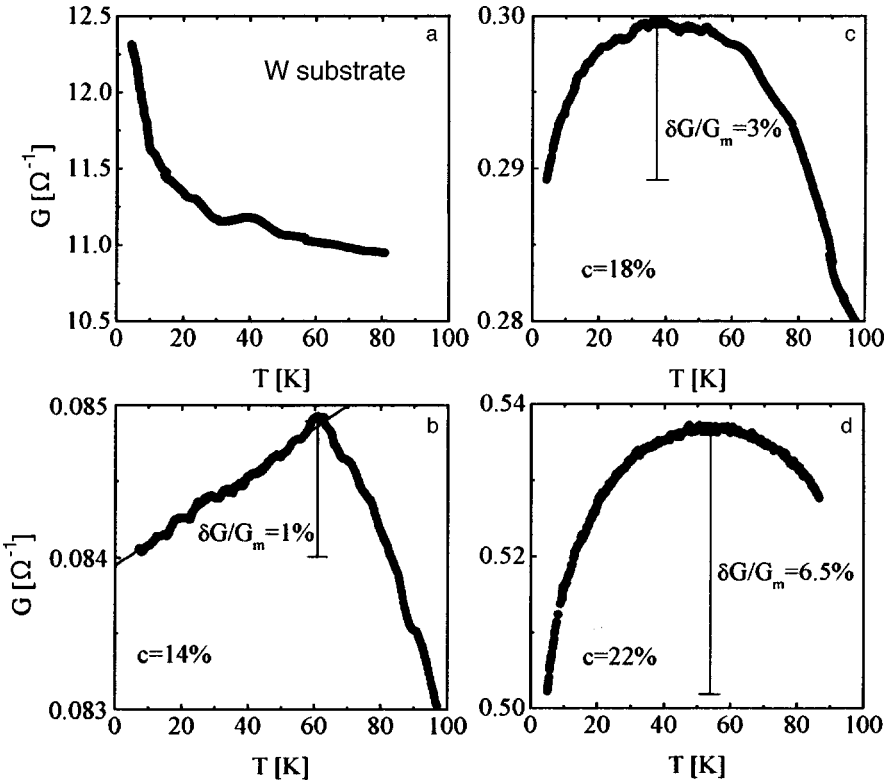


FIG. 2. Temperature dependence of the conductance of structures: a — no $a$-$Si_{1-c}Mn_c$ layer (top contact deposited on the tungsten film); b–d — Mn concentration in a porous $a$-$Si_{1-c}Mn_c$ layer with $c=14\%$ (b), $c=18\%$ (c), and $c=22\%$ (d).

Figure 2 displays the temperature dependences of the conductance of structures containing layers of porous $a$-$Si_{1-c}Mn_c$ ($c=14\%$ (b), $c=18\%$ (c), and $c=22\%$ (d)) as well as structures without a deposited amorphous silicon film[b)] (a). One can see that the conductance of the sample containing no $a$-$Si_{1-c}Mn_c$ is high and remains metallic down to the lowest temperatures. The conductance of the porous $a$-$Si_{1-c}Mn_c$ layers decreases with the impurity concentration (b–d). Measurements performed in a similar geometry on samples not subjected to electrolysis (bulk 3D $a$-$Si_{1-c}Mn_c$ layers) showed that in this case the resistance of a structure is determined by the resistance of the tungsten film. Hence, the conductance of porous layers is much lower than that of compact films.

We shall now analyze the temperature dependence of the conductance $G(T)$. The ''classic'' metallic behavior is observed at high temperatures. At $T=40-60$ K the conductance of the porous layers reaches a maximum value $G_m$ and then decreases as predicted by the theory of weak localization. The relative change in $G$ at $T=4.2$ K reaches $\delta G/G_m \approx 6.5\%$ for the sample with the maximum impurity content.

In the sample with $c=14\%$ $G \propto T$ at low temperatures. It is well known that the linear growth of the conductance with temperature is due to inelastic electron–electron collisions in a 3D system (Landau–Baber scattering).[11] In structures with a high impurity

TABLE I.

| $c$,% | $k_F$, $10^7$ cm$^{-1}$ | $\xi_{\rm loc}$, nm | $L_\varphi$, nm | $L_\varphi/b$ |
|---|---|---|---|---|
| 14 | 7.4 | 185–474 | 1.8–4.7 | 0.36–0.59 |
| 18 | 8.1 | 200–510 | 6–15 | 1.2–1.9 |
| 22 | 8.6 | 215–550 | 14–36 | 2.8–4.5 |

content the temperature dependence $G(T)$ is of a different character. Let us estimate the ratio of the coherence length and the diameter of the wires assuming 1D localization in the silicon wires. According to Ref. 12, the interference correction in a 1D system is determined by the ratio of $L_\varphi$ to the effective localization radius $\xi_{\rm loc}$:

$$\delta G/G_m = L_\varphi/\xi_{\rm loc}. \tag{1}$$

For a wire of finite thickness $\xi_{\rm loc} \approx l(bk_F)^2$ (Ref. 2). Then we obtain from Eq. (1)

$$\frac{L_\varphi}{b} \approx \frac{\delta G}{G_m}(k_F)(k_F l). \tag{2}$$

For purposes of estimation we can take $k_F l \approx 1$ near an Anderson transition. The Fermi momentum is given by the relation $k_F = (3\pi^2 n)^{1/3}$, where $n$ equals twice the Mn concentration, since in silicon Mn is a double acceptor. The computational results for $b = 5-8$ nm are presented in Table I. It is evident from the table that localization does indeed become one-dimensional in structures with manganese content above 14%. The coherence length itself is $L_\varphi \approx 14-36$ nm for the most heavily doped sample. This is close to the value $L_\varphi = 36$ nm at $T = 10$ K, obtained in the analysis of 3D conductance in compact $a$-$Si_{1-c}Mn_c$ films.[9]

For an isolated 1D wire in the weak localization regime, neglecting the correction due to the interaction,[1]

$$G(T) = G_0 - \frac{e^2}{\hbar}\frac{L_\varphi(T)}{b^2}. \tag{3}$$

The temperature dependence of the coherence length in the absence of spin-flip scattering and spin-orbit interaction is determined by the temperature dependence of the inelastic collision time $\tau_{in}$: $L_\varphi(T) = \sqrt{D\tau_{in}(T)}$, where $D$ is the diffusion coefficient. Ordinarily, $\tau_{in}$ decreases with increasing $T$ as $T^{2p}$, so that $G(T) = G_0 - \alpha T^{-p}$, where $\alpha$ is a parameter and $p$ is determined by inelastic scattering. A least-squares fit of this expression to the experimental data for our samples gave $p = 0.31 \pm 0.01$ for $c = 18\%$ and $p = 0.37 \pm 0.01$ for $c = 22\%$. Figure 3 demonstrates the existence of a dependence close to $T^{-1/3}$ at low temperatures. According to theoretical calculations,[13] electron–electron collisions in 1D systems with small energy transfer lead to such a law. This agrees with the fact that the scattering of electrons by conduction electrons is the dominant mechanism of collisions in 3D $a$-$Si_{1-c}Mn_c$ layers also.[9]

The estimated effective localization radius is comparable to the thickness of the porous layer (to the length of the silicon wires). In this case the resistance of one wire should be of the order of $\pi^2\hbar/e^2 \approx 40$ k$\Omega$.[12] Taking for the total resistance of the structure with $c = 22\%$ $R = 1/G \cong 2$ $\Omega$, we find that approximately $2\times10^4$ wires connected in

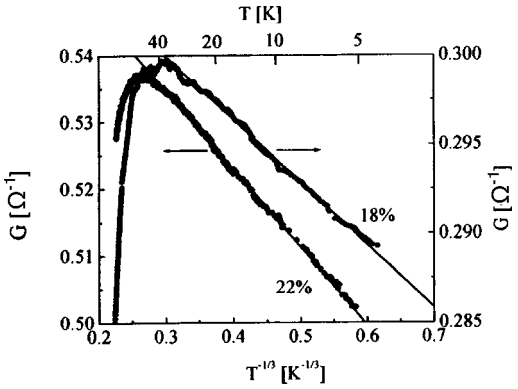


FIG. 3. Conductance versus $T^{-1/3}$ for samples with $c=18\%$ and $c=22\%$.

parallel participate in conduction. This is approximately $10^{-5}$ of all wires in the sample. Hence, most of the wires in a porous film are broken and therefore have a high resistance.

In summary, the decrease observed in the present work in the conductance of porous $a$-$Si_{1-c}Mn_c$ layers at low temperatures can be explained well on the basis of the model of weak electron localization in 1D systems under conditions when interference effects due to electron–electron collisions predominate. This makes the object attractive for investigation of electronic phenomena in low-dimensional disordered structures.

This work was supported by the Russian Fund for Fundamental Research (Grant 97-02-18507).

[a)]e-mail: yakimov@isp.nsc.ru
[b)]The contact pad was deposited directly onto the tungsten film.

[1] P. A. Lee and T. V. Ramakrishnam, Rev. Mod. Phys. **57**, 287 (1985).
[2] A. A. Abrikosov, *Fundamentals of the Theory of Metals*, North-Holland, Amsterdam, 1988 [Russian original, Nauka, Moscow, 1987].
[3] P. Chaudhari and H.-U. Habermeier, Solid State Commun. **34**, 687 (1980).
[4] J. J. Lin and N. Giordano, Phys. Rev. B **35**, 1071 (1987).
[5] W. J. Skocpol, L. D. Jackel, E. L. Hu *et al.*, Phys. Rev. Lett. **49**, 951 (1982).
[6] A. C. Sacharoff and R. M. Westervelt, Phys. Rev. B **26**, 5976 (1982).
[7] Y. Ohno, Y. Nakamura, M. Foley *et al.*, Phys. Rev. B **52**, R11619 (1995).
[8] A. I. Yakimov, A. V. Dvurechenskii, N. P. Stepina *et al.*, J. Phys.: Condens. Matter **9**, 889 (1997).
[9] A. I. Yakimov, A. V. Dvurechenskii, C. J. Adkins, and V. A. Dravin, J. Phys.: Condens. Matter **9**, 499 (1997).
[10] A. I. Yakimov and A. V. Dvurechenskiĭ, JETP Lett. **65**, 354 (1997).
[11] N. F. Mott, *Metal–Insulator Transitions*, Taylor and Francis, London, 1990, p. 258.
[12] D. J. Thouless, Solid State Commun. **34**, 683 (1980).
[13] B. L. Altshuler, A. G. Aronov, and D. E. Khmelnitsky, J. Phys. C **15**, 7367 (1982).

Tranlated by M. E. Alferieff

# On the anomalous *H* dependence of the amplitude of de Haas–van Alphen oscillations in $CeCu_2Si_2$

V. V. Val'kov[a)] and D. M. Dzebisashvili

*Institute of Physics, Siberian Branch of the Russian Academy of Sciences, 660036 Krasnoyarsk, Russia; Krasnoyarsk State University, 660036 Krasnoyarsk, Russia*

(Submitted 15 January 1998)
Pis'ma Zh. Éksp. Teor. Fiz. **67**, No. 4, 270–275 (25 February 1998)

The de Haas–van Alphen effect is studied in heavy-fermion antiferromagnets near the spin-flip transition is studied. It is shown that the strong increase occurring in the amplitude of oscillations near the spin-flip point in an increasing magnetic field, as observed experimentally in $CeCu_2Si_2$, can be explained by strong single-site correlations and magnetic ordering in the subsystem of localized electronic states. © *1998 American Institute of Physics*. [S0021-3640(98)00904-9]

PACS numbers: 75.30.Mb, 75.50.Ee, 71.18.+y

The electronic structure of heavy-fermion compounds remains one of the most intriguing objects in the physics of strongly correlated systems. The appearance of new scenarios of the low-temperature behavior of such substances has stimulated experimental studies directed toward clarifying the structure of their ground state. In this respect the de Haas–van Alphen (dHvA) effect, which makes it possible to determine directly the characteristics of Fermi quasiparticles, plays a special role.

The experimental observation[1–3] of sharp oscillations of the magnetization (which will be referred to below as dHvA oscillations) in a strong magnetic field in heavy-fermion systems has confirmed the existence in them of a Fermi surface and quasi-Fermi excitations at low temperatures. However, the appearance of a number of characteristic features in the oscillatory dependence of the magnetization makes it difficult to analyze the experimental data directly on the basis of the classical Lifshitz–Kosevich theory.[4] For example, the study of the dHvA effect in the heavy-fermion superconductor $CeCu_2Si_2$ has revealed two nontrivial features.[3] First, it was discovered that the period of the dHvA oscillations changes sharply upon transition through the spin-flip point in an increasing magnetic field. The second feature is that the dependence of the amplitude of the dHvA oscillations on the magnetic field $H$ is anomalously strong near the spin-flip transition. In the conventional dHvA effect the amplitude increase becomes appreciable only after a large number of dHvA oscillations, whereas in $CeCu_2Si_2$ a substantial increase in amplitude was observed even for neighboring spikes of the magnetization. This behavior occurred both to the left and right of the spin-flip phase transition point.

$CeCu_2Si_2$ is a heavy-fermion antiferromagnetic superconductor. Long-range antiferromagnetic order is established at low temperatures ($T<T_N\cong 0.5$ K). The dHvA effect is observed in magnetic fields above the second critical field $H_{c2}$, where $CeCu_2Si_2$ was in

 © 1998 American Institute of Physics

the normal state. The low Néel temperature indicates that the exchange-interaction integrals are relatively small. For this reason a quantizing magnetic field gives rise to strong canting of the antiferromagnetic sublattices, while in magnetic fields $H \sim 7$ T a phase transition occurs from the canted antiferromagnetic phase into the collinear ferromagnetic phase. Thus, the dHvA effect in $CeCu_2Si_2$ was observed under conditions of coexistence with a spin-flip phase transition. This fact made it possible to explain the sharp change in the period of dHvA oscillations at a transition through the spin-flip point in conducting antiferromagnets.[5,6] The key factor in the interpretation of the period change was to take into account the strong field dependence of the antiferromagnetic order parameter near the spin-flip point as well as the influence of this parameter on the electronic structure.

In the present letter we report the results of a theoretical study of the dHvA effect in an antiferromagnetic heavy-fermion compound near the spin-flip transition. The main result is an explanation of the anomalously strong increase observed experimentally in $CeCu_2Si_2$ of the dHvA amplitude in an increasing external magnetic field. It is shown that the physical mechanism responsible for this anomaly is the result of the combined effect of strong single-site correlations and long-range magnetic order.

To describe the anomalous increase in the amplitude of the oscillations in $CeCu_2Si_2$ we shall examine a periodic Anderson model that includes, besides the standard terms in the Hamiltonian for this model, interactions leading to the formation of long-range antiferromagnetic order. In this case the Hamiltonian of the system can be written in the form

$$H=\sum_{k\sigma}(\varepsilon_{k\sigma}-\mu)c^{+}_{k\sigma}c_{k\sigma}+\sum_{f\sigma}(E_{0\sigma}-\mu)X^{\sigma\sigma}_{f}+\frac{1}{\sqrt{N}}\sum_{fk\sigma}(V_k\exp(-ikR_f)c^{+}_{k\sigma}X^{0\sigma}_{f} + \text{h.c.})-\frac{1}{2}\sum_{ff'}\mathrm{I}_{ff'}(\mathbf{S}_f\cdot\mathbf{S}_{f'})-J\sum_{f}(\mathbf{S}_f\cdot\vec{\sigma}_f), \quad (1)$$

where the first term describes a system of itinerant electrons with energy $\varepsilon_{k\sigma}=\varepsilon_k - 2\sigma\mu_B H$, $\sigma=\pm 1/2$, and chemical potential $\mu$ in an external magnetic field $H$. The second term in the Hamiltonian describes the subsystem of localized electronic states in the atomic representation: $X^{\sigma\sigma}_f$ and $X^{0\sigma}_f$ are Hubbard operators, $E_{0\sigma}=E_0-\sigma g\mu_B H$, and $E_0$ is the energy of a localized level in the paramagnetic phase. Here, to simplify the exposition we have confined ourselves to the simplest case, where the basis of localized states includes states without electrons and states with one electron and projection of the spin angular momentum on the $z$ axis equal to $\sigma$. The third term in Eq. (1) takes account of the hybridization processes between the collectivized and localized subsystems. The fourth term in the Hamiltonian represents the interaction that gives rise to antiferromagnetic order in the subsystem of localized electrons. $\mathbf{S}_f$ are spin angular momentum vector operators referring to site $f$ in the crystal lattice. Finally, the last term in Eq. (1) takes account of $s-f$ exchange coupling between two groups of electrons.

We shall confine our analysis to magnetic fields in the range to the right of the spin-flip transition point. In this case ferromagnetic ordering of the spin moments is established in the subsystem of localized electronic states. To derive the self-consistency equations describing the low-temperature thermodynamics of the system we employed the Matsubara Green's functions constructed in terms of both conventional Fermi second-quantization operators and Hubbard operators. Besides the standard Fermi diagrammatic technique, the diagrammatic technique for Hubbard operators was also used. Without

going into computational details, we present the system of equations for the thermodynamic averages, leading to renormalizations of the parameters of the electronic structure in the ferromagnetic phase:

$$\langle X^{\sigma\sigma}\rangle = \exp(-(\tilde{E}_\sigma - \mu)/T)/Z + \frac{1}{N}\sum_k (\psi_{k\sigma} - 2\sigma\phi_k), \tag{2}$$

where

$$Z = 1 + \exp(-(\tilde{E}_\uparrow - \mu)/T) + \exp(-(\tilde{E}_\downarrow - \mu)/T),$$

$$\psi_{k\sigma} = \frac{E^+_{k\sigma} - \tilde{\varepsilon}_{k\sigma}}{2\nu_{k\sigma}} f\left(\frac{E^+_{k\sigma} - \mu}{T}\right) + \frac{\tilde{\varepsilon}_{k\sigma} - E^-_{k\sigma}}{2\nu_{k\sigma}} f\left(\frac{E^-_{k\sigma} - \mu}{T}\right) - f\left(\frac{\tilde{E}_\sigma - \mu}{T}\right),$$

$$\phi_k = n_k - \left(\exp\left(\frac{\overline{H}}{T}\right) - 1\right)^{-1}, \quad n_k = (\exp(\omega_k/T) - 1)^{-1}, \quad f(x) = (\exp(x) + 1)^{-1}.$$

The renormalized energy parameters appearing in these expressions have the form $\tilde{E}_\sigma = E_0 - \sigma\overline{H}$, $\tilde{\varepsilon}_{k\sigma} = \varepsilon_{k\sigma} - \sigma JR$, and $\overline{H} = g\mu_B H + I_0 R + J\langle\sigma^z\rangle$. The mixon spectrum associated with the hybridization interaction is described by the formulas

$$E^\pm_{k\sigma} = (\tilde{E}_\sigma + \tilde{\varepsilon}_{k\sigma})/2 \pm \nu_{k\sigma}, \quad \nu_{k\sigma} = ((\tilde{E}_\sigma - \tilde{\varepsilon}_{k\sigma})^2/4 + K_\sigma V_k^2)^{1/2}.$$

For what follows it is important that strong single-site correlations renormalize the effective hybridization interaction constant. Formally, this appears as the factor $K_\sigma = \langle X^{\sigma\sigma}\rangle + \langle X^{00}\rangle$ in the radicand in the expression for $\nu_{k\sigma}$. This renormalization is strongest in the saturated ferromagnetic state, where $K_\uparrow = 1$ while $K_\downarrow = 0$. In this case the hybridization channel remains completely open for electrons with spin moment oriented in the direction of the field, while for electrons with the opposite spin polarization the hybridization processes are completely suppressed. However, since hybridization mixing strongly influences the effective mass of a Fermi quasiparticle, the above-noted renormalization of the hybridization constant strongly influences the amplitude of the dHvA effect. Specifically, a change in the degree of ordering in the subsystem of localized electronic states will affect the dHvA amplitude.

To calculate the dHvA effect in a right-hand neighborhood of the spin-flip transition under conditions of hybridization mixing of itinerant and localized electronic states we shall employ the technique of summing over the Matsubara frequencies with the electron propagators represented in the form of contour integrals in the complex region.[7] This technique for magnetically ordered semiconductor systems was used in Ref. 8. In our case the oscillatory part of the magnetization of itinerant electrons can be written in the form

$$M_\sim = -\sum_\sigma \sum_{k=1}^{\infty} \sum_{\omega_n > 0} \frac{(-1)^k}{\sqrt{k}} A_{k\sigma}(\omega_n) \sin\left(2\pi k \frac{\tilde{\mu}_{n\sigma}}{\hbar\omega_c} + \varphi_\sigma\right), \tag{3}$$

where the ''partial'' amplitudes are determined by the expression

$$A_{k\sigma}(\omega_n) = \left(\frac{TVe\tilde{\mu}_{n\sigma}}{\pi\hbar^2 c}\right)\left(\frac{m_\parallel}{\hbar\omega_c}\right)^{1/2} \exp\left(-\frac{2\pi k\omega_n\alpha_{n\sigma}}{\hbar\omega_c}\right), \quad \alpha_{n\sigma} = 1 + \Gamma_{n\sigma},$$

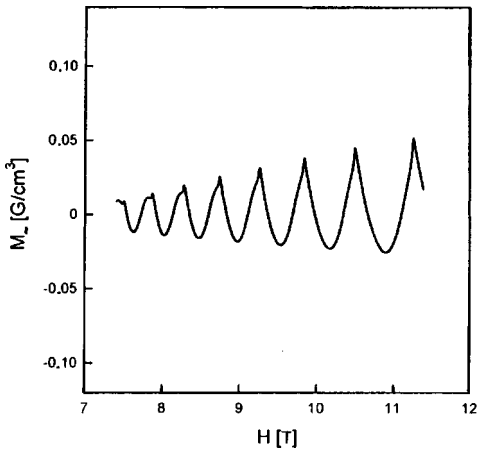


FIG. 1. Oscillatory part of the magnetization in a right-hand neighborhood of the spin-flip transition in a heavy-fermion antiferromagnet.

$$\Gamma_{n\sigma}=K_{\sigma}|v|^2\{\omega_n^2+(\widetilde{E}_{\sigma}-\mu)^2\}^{-1}, \quad \widetilde{\mu}_{n\sigma}=\mu+\sigma JR+(\widetilde{E}_{\sigma}-\mu)\Gamma_{n\sigma}. \tag{4}$$

The results obtained by solving the self-consistent equations for the averages $\langle X^{\sigma\sigma}\rangle$, the chemical potential $\mu$, and $\langle\sigma^z\rangle$ numerically enabled us to analyze on the basis of Eqs. (3) and (4) the dHvA effect in a right-hand neighborhood of the spin-flip transition. Figure 1 shows the oscillatory part of the magnetization of itinerant electrons calculated in this manner. The following values of the model parameters were used in the calculations: $J=0.5$ eV, $V=0.05$ eV, $T=0.1$ K, $m=0.1m_0$, $I_0=-8.1\times10^{-4}$ eV, and $E_0=0.3$ eV. The choice of values for some of the parameters was dictated, specifically, by experimental data on $CeCu_2Si_2$. Thus, for example, $H_c\cong 7$ T, while the period of the oscillations was matched by varying the parameters to the value in the experiment of Ref. 3. The position of the localized level was fixed so as to obtain a high electronic specific heat. The oscillations displayed in Fig. 1 are due to only one spin subband, corresponding to the characteristic electron magnetic moment being oriented antiparallel to the magnetic field. The amplitude of the magnetization oscillations due to the other spin subband is very small, and the corresponding contribution to the dHvA effect is absent. One can see that as the magnetic field increases, strong growth of the amplitude of the dHvA oscillations occurs with neighboring spikes in the magnetization differing in amplitude by a substantial amount.

The physical mechanism of the anomalous growth of the amplitude involves the following. At the point of the spin-flip transition the gap in the spin-wave excitations spectrum equals zero. For this reason thermal excitation of spin waves occurs relatively easily. This results in an appreciable decrease of the magnetization. As the magnetic field increases, the gap in the spin-wave excitation spectrum increases. Such an increase in the activation energy greatly decreases the density of thermally excited magnons. For this reason the magnetization tends toward its maximum value.

Magnetic ordering in the subsystem of localized electronic states lifts the degeneracy of these states in the direction of the spin moment. Since the energy splitting $\widetilde{E}_{\downarrow} - \widetilde{E}_{\uparrow}$ is much higher than the temperature, only levels corresponding to an orientation of the localized magnetic moment in a direction collinear with the magnetic field are occupied. This circumstance together with the presence of strong single-site electronic correlations determine the different intensities of the hybridization processes for itinerant and localized electrons. Thus, the hybridization scattering channel for electrons spin-polarized in the direction of the field remains open. For this reason, the electronic states of the corresponding spin subbands are strongly hybridized and have a large effective mass (the chemical potential lies near the value of $\widetilde{E}_{\uparrow}$). This results in a high electronic specific heat at low temperatures.

A different situation arises for electronic states with the opposite orientation of the spin moments. For these states the renormalization of the hybridization constant on account of Hubbard correlations becomes so large that substantial (in the limiting case complete) suppression of the hybridization scattering channel occurs. Electronic states with such (negative in what follows) polarization of the spin moment remain weakly hybridized. The amplitude of the dHvA effect for them remains high enough so that sharp oscillations of magnetization in an increasing magnetic field can be recorded experimentally. The thermal excitation of magnons gives rise to an increase in the average $\langle X^{\downarrow\downarrow} \rangle$, which in turn increases the effective hybridization constant for electrons with ''down'' spin. For this reason, as temperature increases, the amplitude of the dHvA oscillations decreases rapidly, as is observed experimentally in all heavy-fermion compounds. The picture is reversed if $\langle X^{\downarrow\downarrow} \rangle$ decreases for any reason. This can be achieved, for example, by increasing the external magnetic field. Such an effect of a magnetic field is especially effective near a spin-flip transition. Indeed, for a relatively small change in field $H$ from $H = H_c$ to a value of $H$ such that $H - H_c \gg T$ the activation energy of magnons increases to such an extent that there are no spin-wave excitations in the system and $\langle S^z \rangle$ approaches its maximum value, while the effective hybridization constant for electrons with negative spin polarization approaches zero. This is the reason for the anomalously rapid increase of the amplitude of dHvA oscillations.

As temperature increases, the above-discussed anomaly of the $H$ dependence of the dHvA amplitude will become larger. This is due to the increasing number of thermally excited magnons. For this reason, as $H$ increases from $H = H_c$ to $H - H_c \gg T$ the magnetization will change by a large amount. As a result, the relative change in amplitude of the oscillations will also become large.

In conclusion, we note that the above-examined mechanism of the anomalous $H$ dependence of the amplitude of the oscillations will operate in all antiferromagnetic heavy-fermion compounds with low Néel temperatures. It is important only that the field $H_c$ at which the spin-flip transition occurs lie in the range where the dHvA effect is observed. Significantly, investigation of this anomaly will yield, besides the standard information about the properties of a Fermi system, additional information about the magnetically ordered subsystem of localized states.

This work was supported by the Krasnoyarsk Region Science Fund (Grant 6F0150).

[a)]e-mail: vvv@iph.krasnoyarsk.su

---

[1] P. H. P. Reinders, M. Springford, P. T. Coleridge *et al.*, Phys. Rev. Lett. **57**, 1631 (1986).
[2] L. Taillefer and G. G. Lonzarich, Phys. Rev. Lett. **60**, 1570 (1988).
[3] M. Hunt, P. Meeson, P. A. Probst *et al.*, J. Phys.: Condens. Matter **2**, 6859 (1990).
[4] I. M. Lifshits, M. Ya. Azbel', and M. I. Kaganov, *Electron Theory of Metals*, Consultants Bureau, New York, 1973 [Russian original, Nauka, Moscow, 1971].
[5] V. V. Val'kov and D. M. Dzebisashvili, Fiz. Tverd. Tela (St. Petersburg) **39**, 204 (1997) [Phys. Solid State **38**, 179 (1997)].
[6] V. V. Val'kov and D. M. Dzebisashvili, Fiz. Met. Metalloved. **84**, 30 (1997).
[7] A. Wasserman, M. Springford, and A. C. Hewson, J. Phys.: Condens. Matter **1**, 2669 (1989).
[8] V. V. Val'kov and D. M. Dzebisashvili, Zh. Éksp. Teor. Fiz. **111**, 654 (1997) [JETP **84**, 360 (1997)].

Translated by M. E. Alferieff

# Vortex drag in the quantum Hall effect

S. A. Vitkalov
*Chemistry Department, University of Florida*

(Submitted 21 January 1998)
Pis'ma Zh. Éksp. Teor. Fiz. **67**, No. 4, 276–279 (25 February 1998)

A new model of momentum and electric field transfer between two adjacent 2D electron systems in the quantum Hall effect is proposed. The drag effect is due to momentum transfer from the vortex system of one layer to the vortex system of another layer. The remarkable result of this approach is a periodic change of sign of the dragged electric field as a function of the difference between the layer filling factors. © *1998 American Institute of Physics.* [S0021-3640(98)01004-4]

PACS numbers: 73.40.Hm

The drag effect in double-layer two-dimensional electron systems has been the subject of intense recent interest, especially at high magnetic fields, where the quantum Hall effect (QHE) exists.[1] Theoretical explanations of the observed drag effect mostly reduce to the ordinary Coulomb interaction between electrons occupying the Landau levels in the two layers.[2] These explanations are not much related to the quantum Hall effect. In the present letter a new mechanism for the momentum transfer between the layers is proposed, which exists exclusively under QHE conditions. For simplicity we shall consider integer filling factors.

The model is based on a treatment of the quantum Hall liquid as a superfluid state of Chern–Simons charged bosons.[3,4] The ground state $\phi=\phi_1+i\phi_2$ has a quasilong-range phase correlation[5] and is uniform in the mean field approximation at ''magic'' filling factors $\nu_i^0=i$, where $i=1, 2\ldots$ is an integer.

In accordance with this point of view on the QHE, vortex ($H>H_i^0$) or antivortex ($H<H_i^0$) excitations are created away from the filling factor $\nu_i^0$, with concentrations $N_i^v=|H-H_i^0|/\Phi_0$, where $H$ is the external magnetic field, and $H_i^0$ is the magnetic field corresponding to the filling factor $\nu_i^0$. The magnetic flux carried by the vortex (antivortex) is $\Phi_0$ ($-\Phi_0$), where $\Phi_0=hc/e$ is the flux quantum. If the ground state carries a supercurrent $\mathbf{j}^{\text{ext}}$ the vortices experience an average force $\mathbf{F}^{\text{ext}}$, which corresponds to the force acting on the vortices in an ordinary superconductor. Formally the force is a result of current–current interactions between the external supercurrent $\mathbf{j}^{\text{ext}}$ and the vortex supercurrent $\mathbf{j}^v$ (Ref. 6). The Hamiltonian of the interaction is $H_{\text{int}}=\Lambda(\mathbf{j}^v\cdot\mathbf{j}^{\text{ext}})$, where $\Lambda$ is an interaction constant. The negative of the derivative of the Hamiltonian $H_{\text{int}}$ with respect to the vortex position is the external force $\mathbf{F}^{\text{ext}}$. The gauge invariant expression for the supercurrent of charged bosons is the same as for an ordinary superconductor, but the charge of the Cooper pair $2e$ needs to be changed to the boson charge $q$. The charged boson supercurrent is $\mathbf{j}=-(\Lambda c)^{-1}(\mathbf{A}-hc/2\pi q\nabla\chi)$, where $\chi$ is the phase of the boson

 © 1998 American Institute of Physics

ground state $\phi$. Assuming that the function $\phi$ is single-valued, we find the external force $F^{\text{ext}}$ to be

$$\mathbf{F}^{\text{ext}}=\frac{\pm\Phi_0}{q_i c}[\mathbf{j}^{\text{ext}}\times\mathbf{e}_z], \tag{1}$$

where $c$ is the speed of light, $\mathbf{e}_z$ is the direction of the magnetic field $\mathbf{H}$, and the sign $+$ $(-)$ corresponds to the vortex (antivortex). The value $q_i$ is the boson charge in units of the electron charge: $q=q_i e$. A similar expression for the force in an external electric field $\mathbf{E}$ has been found in a different approach:[7]

$$\mathbf{F}_2^{\text{ext}}=\frac{e^2}{hc}\Phi_0\mathbf{E}. \tag{1a}$$

Using the relation between the current and the electric field in the QHE: $j^{\text{ext}}=\sigma_{xy}E=q_i\times e^2/hE$, we obtain $F^{\text{ext}}=F_2^{\text{ext}}$.

There are several possibilities for the vortex motion in the external current $\mathbf{j}^{\text{ext}}$. A simple picture is considered here. At the temperature $T=0$ K all the vortices are pinned by the disorder, and the current $\mathbf{j}^{\text{ext}}$ flows without any dissipation. There is no momentum transfer to the vortex system at $T=0$ K. At a finite temperature $T>0$ K, the vortices can jump from one point to another as a result of thermal fluctuations. The external current $\mathbf{j}^{\text{ext}}$ induces an average momentum (creep) of the vortices in the direction of the force $\mathbf{F}^{\text{ext}}$. Thus, at the temperature $T>0$ K there is momentum transfer from the external current to the vortex system. The average nonzero momentum of the vortices in the first layer will relax and be partially converted into momentum of the vortices of the second layer. Actually, the most effective channel of momentum transfer between the layers is not clear. A suitable candidate is the phonon system.

In this paper the momentum transfer between the layers is studied phenomenologically. Let us consider the momentum transfer between the vortices at some QHE resistance minimum of the first layer ($H_1^0$) and the vortices at some QHE resistance minimum of the second layer ($H_2^0$) (see Fig. 1). The average momentum of the vortices in the first (second) layer is $\mathbf{P}_1$ ($\mathbf{P}_2$). The total force exerted on the vortex system by the external current $\mathbf{j}^{\text{ext}}$ (the layers are squares of unit area) is $N_i^v\mathbf{F}_i^{\text{ext}}$ (1), where $i=1,2$ is the layer index now.

Newton's equations for the momenta of the vortices are ($H-H_i^0=N_i^v\Phi_0$):

$$d\mathbf{P}_1/dt=1/(q_1 c)[\mathbf{j}_1^{\text{ext}}\times(\mathbf{H}-\mathbf{H}_1^0)]-\mathbf{P}_1/\tau_1-\mathbf{F}^{\text{int}}, \tag{2}$$

$$d\mathbf{P}_2/dt=1/(q_2 c)[\mathbf{j}_2^{\text{ext}}\times(\mathbf{H}-\mathbf{H}_2^0)]-\mathbf{P}_2/\tau_2+\mathbf{F}^{\text{int}}, \tag{3}$$

where the $\tau_i$ are the momentum relaxation rates and $\mathbf{F}^{\text{int}}$ is the interlayer drag force.

In the experiment of Ref. 1 an additional electric field $\mathbf{E}_2^{\text{ext}}$ was applied to the second layer to cancel the current $\mathbf{j}_2^{\text{ext}}$. In this case Eq. (3) is transformed into

$$d\mathbf{P}_2/dt=-\mathbf{P}_2/\tau_2+\mathbf{F}^{\text{int}}. \tag{3a}$$

For small perturbations of the vortex distribution function the interlayer drag force is proportional to the vortex momentum $\mathbf{P}_1$. At a small value of vortex concentration $N_2^v$, the total drag force is proportional to the concentration $N_2^v$. Therefore the interlayer drag force $\mathbf{F}^{\text{int}}$ can be approximated by

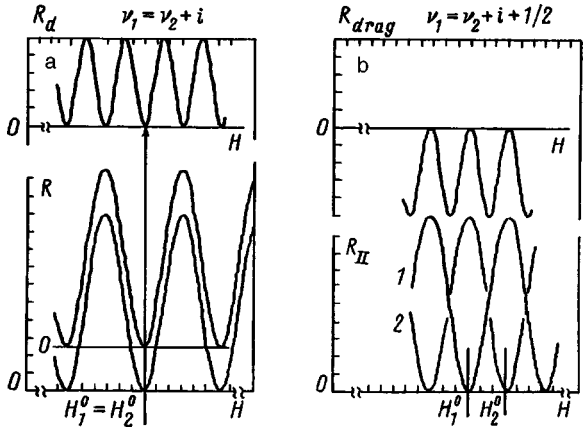


FIG. 1. Dependence of the drag resistance $R_{\rm drag}=E_2/j_1^{\rm ext}$ on the magnetic field $H$ in a bilayer 2D electron system under conditions of the quantum Hall effect. The sign of $R_{\rm drag}$ is positive in the case of filling factors $\nu_1=\nu_2+i$ and negative in the case of filling factors $\nu_1=\nu_2+i+1/2$, where $i$ is an integer and 1,2 are layer indices.

$$\mathbf{F}^{\rm int}=\alpha N_2^v\mathbf{P}_1\,, \tag{4}$$

where $\alpha$ is a constant.

Since the interlayer drag force $F^{\rm int}$ is much less than the external force $F^{\rm ext}$, the former can be taken as a small perturbation in Eq. (2). From Eqs. (2), (3a), and (4) the dragged momentum of the vortices $\mathbf{P}_2$ is found to be

$$\mathbf{P}_2=\frac{\alpha\tau_1\tau_2}{q_1c}[\mathbf{j}_1^{\rm ext}\times(\mathbf{H}-\mathbf{H}_1^0)]N_2^v. \tag{5}$$

In accordance with Maxwellian electrodynamics the electric field generated by the vortex movement is $\mathbf{E}_2=1/c[(\mathbf{H}-\mathbf{H}_2^v)\times\mathbf{V}_2]$, where $\mathbf{V}_2$ is the average vortex velocity in the second layer. The external electric field $\mathbf{E}_2^{\rm ext}$ should cancel the electric field $\mathbf{E}_2$ to prevent a net current $j_2^{\rm ext}$: $\mathbf{E}_2+\mathbf{E}_2^{\rm ext}=0$.

Using the expression $\mathbf{P}_2=m_vN_2^v\mathbf{V}_2$, where $m_v$ is a mass of the vortex, the dragged electric field in the second layer is found to be:

$$\mathbf{E}_2=g\mathbf{j}_1^{\rm ext}(H-H_1^0)(H-H_2^0), \tag{6}$$

where $g=\alpha\tau_1\tau_2/q_1m_vc^2$ is a constant.

1) Let us consider the case of filling factors $\nu_1=\nu_2+i$ (Fig. 1a), where $i$ is an integer (for example, equal electron concentrations $n_1^e=n_2^e$ in both layers). In this case the electric field in the second layer is

$$\mathbf{E}_2=g\mathbf{j}_1^{\rm ext}(H-H_1^0)^2. \tag{7}$$

In Eq. (7) the drag voltage has a quadratic dependence on the magnetic field deviation from the QHE resistance minimum $H_1^0$. Far from the minimum $H_1^0$ the phase-coherent

ground state $\phi$ is destroyed and the vortex drag disappears. Thus each QHE minimum is accompanied by two peaks of the drag voltage $E_2$ on different sides of the minimum $H_1^0$. This behavior correlates with the experiment of Ref. 1.

2) Let us assume that the QHE resistance minima $H_1^0$ and $H_2^0$ in the layers do not coincide with each other (Fig. 1b). In this case, in accordance with Eq. (6), the electric field $E_2$ changes sign in the interval $H_1^0<H<H_2^0$. This happens because the antivortices ($H<H_2^0$) are dragged by the vortices ($H>H_1^0$).

If we fix the electron concentration $n_1^e$ in the first layer and vary the concentration $n_2^e$ in the second layer, the sign of the dragged voltage will oscillate on account of the periodicity of the QHE conditions with respect to the electron concentration $n_e$ (Ref. 8). The main cause of the sign variations is the periodic change of the ground state excitations from vortices to antivortices with respect to changes in the electron concentration or the external magnetic field.

In conclusion, the vortex model of the drag effect in a bilayer two-dimensional electron system is proposed. Arising exclusively under conditions of the quantum Hall effect, the drag effect is induced by momentum transfer from the vortex excitations of the ground state of the first layer to the vortex excitations of the ground state of the second layer. At equal electron concentrations in the layers the dragged voltage has a double-peak structure, in agreement with experiment.[1] For vortex–vortex or antivortex–antivortex momentum transfer the sign of the external electric field in the second layer is opposite to the sign of the electric field in the first layer, in accordance with the experiment of Ref. 1. For vortex–antivortex or antivortex–vortex momentum transfer the sign of the external electric field in the second layer is the *same* as the sign of the electric field in the first layer.

This work was supported by the National Science Foundation under Grant CHE-9624243.

[1] H. Rubel, A. Fisher, W. Dietsche *et al.*, Phys. Rev. Lett. **78**, 1763 (1997).
[2] M. C. Bonsager, K. Flensberg, B. Yu-Kuang Hu, and Antii-Pekka Janho, Phys. Rev. Lett. **77**, 1366 (1996).
[3] S.-C. Zhang, Int. J. Mod. Phys. B **6**, 25 (1992).
[4] S. Kivelson, D.-H. Lee, and S.-C. Zhang, Phys. Rev. B **46**, 2223 (1992).
[5] S. M. Girvin and A. H. Macdonald, Phys. Rev. Lett. **58**, 1252 (1987).
[6] A. A. Abrikosov, *Principles of the Theory of Metals* [in Russian], Nauka, Moscow, 1985, p. 396.
[7] J. E. Avron and P. G. Zograf, http://xxx.lanl.gov/abs/cond-mat/9711177.
[8] K. von Klitzing, G. Dorda, and M. Pepper, Phys. Rev. Lett. **45**, 494 (1980).

Published in English in the original Russian journal. Edited by Steve Torstveit.

# Observation of the pre-explosion state and of the initial moment of an explosion of a field emission center in a field emission microscope

A. V. Batrakov,[a] S. A. Popov, and D. I. Proskurovskiĭ
*Institute of High-Current Electronics, Siberian Branch of the Russian Academy of Sciences, 634055 Tomsk, Russian*

(Submitted 9 January 1998)
Pis'ma Zh. Éksp. Teor. Fiz. **67**, No. 4, 280–285 (25 February 1998)

Never-before-observed emission images corresponding to a transition from intense field emission to explosive electron emission are obtained in a Müller field emission microscope with short ($\sim 2$ ns) high-voltage pulses. These images are much brighter than ordinary field emission images. Moreover, the images have a characteristic multi-brightness structure with ring-shaped frames around regions of different brightness. Analysis of the experimental data points to a field emission nature of these images. The appearance of such emission images can be explained by emission from a liquid phase which arises immediately prior to the explosion of a microemitter. © *1998 American Institute of Physics.* [S0021-3640(98)01104-9]

PACS numbers: 61.16.Fk, 07.78.+s

The transition from field emission (FE) to explosive electron emission (EEE) or, as previously thought, to a ''vacuum arc'' has been studied in many works. The critical field emission current densities and the electric fields at the cathode that lead to transition to an ''arc'' have been measured,[1,2] a bright ring framing the conventional emission image has been observed in the ''prebreakdown phase,''[1,2] the dependences of the delay time of the emitter explosion on the field emission current density have been measured,[3,4] and calculations of both the heating of the field emitter in the prebreakdown stage[5,6] and the heating of the microtip by the field emission current itself[5,7] have been performed.

Nonetheless, the entire sequence of pre-explosion phenomena occurring at the field emitter has by no means been thoroughly studied. Specifically, since the appearance of a liquid phase at the tip of the emitter can precede the explosive breakdown of the emitter,[8] it is entirely natural to conjecture that the development of electrohydrodynamic phenomena should complicate the scenarios of the transition to explosion. However, thus far only limited reliable experimental data on the dynamics of the pre-explosion processes immediately prior to an explosion are available. The transition from FE with high current densities to an explosion of the field emitter occurs so rapidly that it has proved impossible thus far to distinguish separate phases of this process. For this reason, for analysis of the experiments this transition is assumed to be instantaneous. The theory attempts to describe this process.

 © 1998 American Institute of Physics

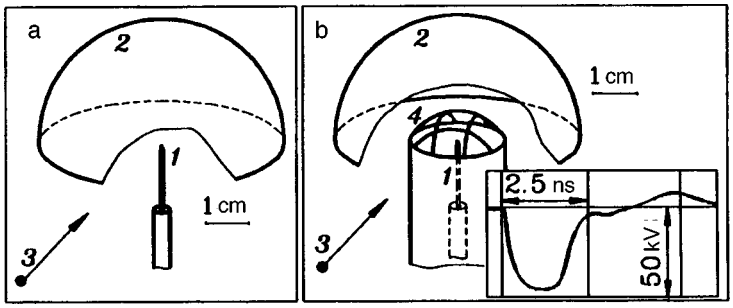


FIG. 1. Two-electrode (a) and three-electrode (b) designs of Müller field emission microscopes employed in the experiments and a typical oscillogram of a minimum-duration voltage pulse applied to the cathode: *1* — tip electrode; *2* — luminescent screen; *3* — point of observation of the images; *4* — four-wire grid.

In the present work we endeavored to record, using a Müller field emission microscope, the emission corresponding to a transitional state between FE and EEE. As far as we know, a transition from FE to EEE in a Müller field emission microscope has never been observed directly. Apparently, this is due to the high intensity of phosphorescence of the luminescent screen and the long persistence time of the screen, which ''stores'' information about the processes occurring in the emission zone. However, one can attempt to obtain information about the structure of the emission zone immediately prior to the explosion of a microemitter by using short voltage pulses of duration $\sim 10^{-9}$ s.

A schematic diagram of the field emission microscopes used in the experiments is displayed in Fig. 1. A tungsten tip with a radius of curvature $\sim 5$ $\mu$m served as the cathode. A metallic hemisphere with a radius of 2.7 cm, whose inner surface was coated with a phosphor, served as the anode of the microscope. The experiments were performed in a $10^{-6}$–$10^{-5}$ Pa oil-free vacuum. Voltage pulses with a regulable duration (2–10 ns) and amplitude up to 50 kV were applied to the cathode. The cathode surface was first cleaned by prolonged conditioning breakdowns using 10 ns, 50 kV pulses.

Next, 2 ns voltage pulses with amplitude gradually increasing from pulse to pulse were applied to the cathode. At some voltage ($\sim$40 kV) emission images characteristic for field emission from microemitters, which formed on the tip of the cathode after the vacuum breakdowns, appeared.[9–11] These images had a low brightness and were reproduced well from pulse to pulse (Fig. 2a). We shall call them type-I images.

A small increase in the amplitude of the voltage pulses (by 1–2 kV) resulted in a radical change in the character of the emission images. The images consisted of bright spots, whose phosphorescence was of a concentric, step character with a ring-shaped frame around regions of different brightness (Fig. 2b–e) (type-II emission images). However, in contrast to previously observed images with rings,[1,2] in the present case the ring-shaped structures appeared not only at the periphery but also inside the images (Fig. 2b,d).

The type-II emission images were not reproduced from pulse to pulse. In addition, the type-I emission images changed radically after each appearance of a type-II emission image, attesting to a change in the microgeometry of the surface of the cathode tip. We also note that as the amplitude of the voltage pulses increases, the transition from type-I

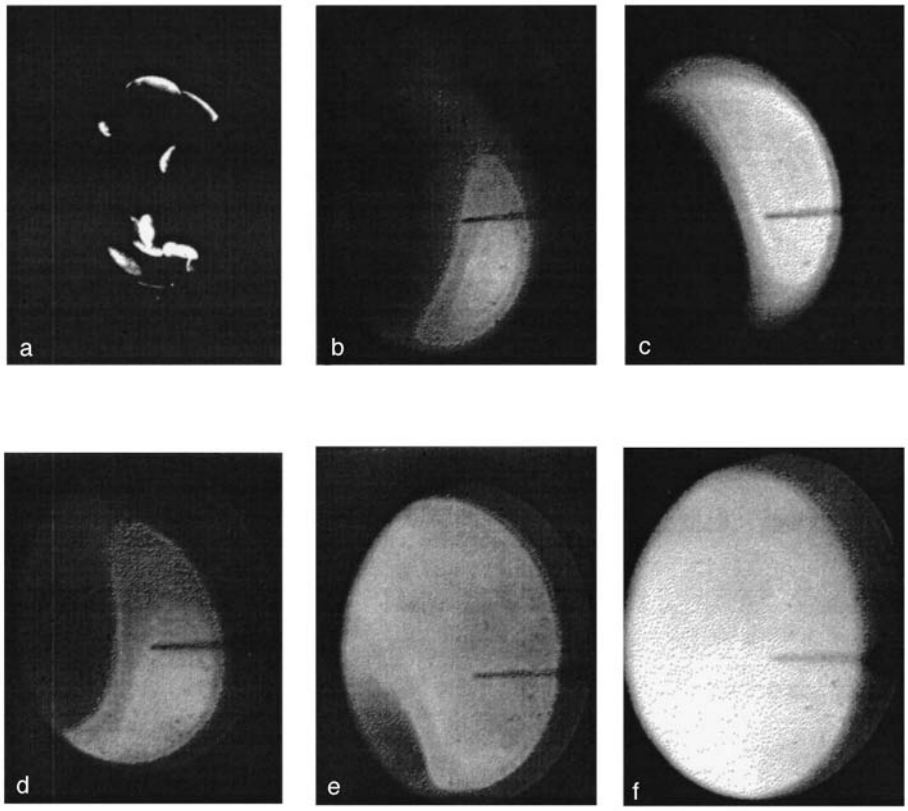


FIG. 2. Typical type-I image (a) obtained with exposure to 50 field emission current pulses and typical single type-II (b–e) and type-III (f) images.

to type-II emission images is very sharp — images with an intermediate form and intermediate luminescence intensity are not formed. When the duration of the voltage pulses was increased above 5–7 ns, type-II images could not be observed (including also at lower voltages) because of the intense phosphorescence of a large portion of the screen by the induced-EEE current (type-III images, Fig. 2f). Type-III images also appeared with short ($<5$ ns) pulse durations but a somewhat higher amplitude of the voltage pulses.

Intense phosphorescence, close to the case of type-III images, of the screen phosphor is characteristic of type-II images. The shapes and sizes of type-II images varied over wide limits from pulse to pulse. As the amplitude of the pulses increased gradually, the angular sizes of these images increased on the whole and gradually approached the sizes of type-III images. In the process, the characteristic ring-shaped multibrightness structures in the type-II images gradually vanished.

The continuous transition from type-II to type-III images and the fact that short pulses were required in order to record type-II images indicate that type-II images reflect the transitional state between FE and EEE. This makes it difficult to identify the type of emission corresponding to this state.

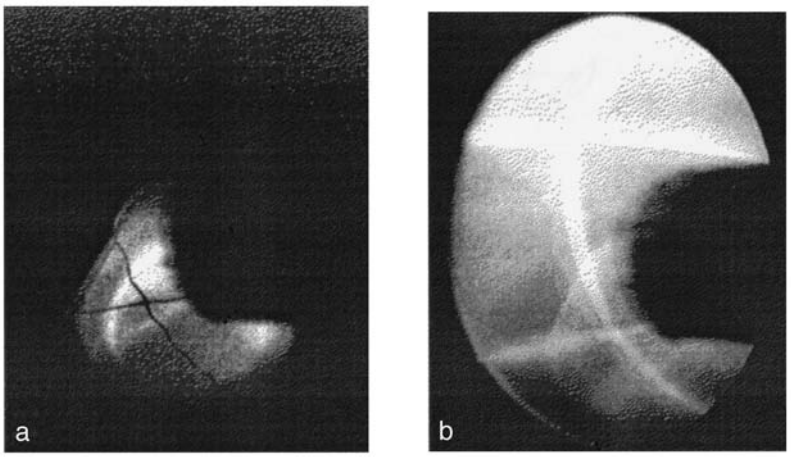


FIG. 3. Single type-II images (a) and type-III images (b) obtained successively in a field emission microscope with the design of the second type.

To determine the nature of type-II images we performed experiments in a field-emission microscope with the second type of construction (Fig. 1), where a grid consisting of 100 $\mu$m wires and having the same potential as the screen was placed between the cathode and the screen. Figure 3 shows photographs of typical type-II and -III images in a field emission microscope with the second type of construction. It is clearly seen that the wires cast shadows in the type-II images, while in the type-III images the shadow region becomes bright.

To clarify the reasons why the dark projection of the wires changes into a bright projection we used the SuperSAM program,[12] which takes account of the space charge of the electrons, to model the electron flow into the microscope. The modeling yielded a relation between the radius of the emission boundary and the distance from a wire to the region of convergence of the electron trajectories. It was found that for an emission region radius of 5 $\mu$m the electron trajectories converge at a distance of $\sim$10 cm, which is much greater than distance from the wires to the screen (1.5 cm). This gives a shadow from the wires. The shadow region transforms into a bright region if the trajectories collect in the space between the wires and the screen. This occurs when the radius of the emission zone becomes greater than the radius of a wire (in our case, 100 $\mu$m), i.e., a cathode plasma arises. This result shows unequivocally that the type-II images correspond to FE while the type-III images correspond to EEE. Since the lifetime of the EEE cannot be longer than the duration of a voltage pulse (2 ns), we obtain that the expansion rate of the plasma at the initial moment of an explosion of a field emitter is not less than $5\times10^4$ m/s, in good agreement with the results obtained in other investigations.[13]

Summarizing our analysis of type-II images, it can be asserted that they correspond to FE. At the same time, the appearance of type-II images irreversibly changes the microrelief of the surface of the emitter tip. These two factors can be explained, from our standpoint, by the appearance of a liquid phase at the tip of the cathode toward the end of

the voltage pulse. A melt zone apparently forms in locations where effectively emitting microasperities cluster. Since under the conditioning with short EEE pulses the height of such microasperities is small[14] and the microasperities can effectively remove heat, the melt region can encompass an entire cluster. This explains the relatively large sizes of type-II emission images.

Such an approach makes it possible to explain why type-II images are difficult to record with increasing voltage pulse duration. It is known that when

$$2\gamma/r \leqslant \varepsilon_0 E_0^2/2 \tag{1}$$

($\gamma$ is the surface tension, $r$ is the characteristic initial radius of curvature of the surface of the liquid metal (LM), $\varepsilon_0$ is the permittivity of free space, and $E_0$ is the intensity of the electric field at the surface of the liquid metal), a LM asperity forms.[15] For estimated values $E_0 = 5 \times 10^9$ V/m and $r = 5$ $\mu$m, the right-hand side of the inequality (1) is two orders of magnitude greater than the left-hand side. The characteristic formation time $t_0$ of the LM asperity can be estimated, according to Ref. 16, as

$$t_0 = \frac{2\gamma}{E_0^3}\sqrt{\frac{\rho}{\varepsilon_0^3}\ln\left(\frac{2\gamma}{\xi_0 \varepsilon_0 E_0^2}\right)}, \tag{2}$$

where $\xi_0$ is the amplitude of the initial disturbances of the LM surface. Taking $\xi_0 = 0.2r$ (Ref. 17), we find from Eq. (2) that $t_0 \sim 0.1$ ns. Thus the appearance of a melt zone on the cathode tip leads to very rapid formation of a sharp LM asperity, additional enhancement of the electric field, and acceleration of the explosion process. It is obvious that the greater the duration of the high-voltage pulse, the more difficult it will be to ''catch'' this situation. If we did manage to do so and the melt appeared at the end of a voltage pulse, so that an explosion did not occur, then there should be enough time for the LM asperity to break up partially or completely before it crystallizes. In this case, in the course of the experiments the end of the tip should become polished and the voltage at which melt appears on the emitter tip should increase. We indeed observed this, and in order to be able to continue the experiments in an accessible voltage range, the cathode had to be subjected periodically to a current due to EEE initiated by ''long'' (10 ns) 50 kV voltage pulses. This procedure lowered the voltage at which type-II images appeared. This is easily explained by regeneration of microasperities on the cathode tip for such pulse durations.[14]

In summary, the appearance of a liquid phase immediately prior to the initiation of EEE explains quite well the appearance and some characteristics of type-II images. However, the high brightness of type-II images, attesting to a jump in the field emission current density accompanying the appearance of a melt zone, remains unexplained. The nature of the step character of the luminescence of the phosphor in these images and the ring-shaped framing of regions of different brightness also require explanation.

The work was supported by the Russian Fund for Fundamental Research (Project 97-02-17208).

[a)]e-mail: bat@hcei.tomsk.su

[1] W. P. Dyke, J. K. Trolan, E. E. Mastin, and J. P. Barbour, Phys. Rev. **91**, 1043 (1953).
[2] I. L. Sokol'skaya and G. N. Furseĭ, Radiotekh. Élektron. **7**, 1474 (1962).
[3] G. K. Kartsev, G. A. Mesyats, D. I. Proskurovskiĭ *et al.*, Dokl. Akad. Nauk SSSR **192**, 309 (1970) [Sov. Phys. Dokl. **15**, 475 (1970)].
[4] V. M. Zhukov, M. S. Aksenov, G. N. Furseĭ *et al.*, Izv. Akad. Nauk SSSR, Ser. Fiz. **43**, 1310 (1982).
[5] E. A. Litvinov, G. A. Mesyats, and D. I. Proskurovskiĭ, Usp. Fiz. Nauk **139**, 265 (1983) [Sov. Phys. Usp. **26**, 138 (1983)].
[6] D. V. Glazanov, L. M. Baskin, and G. N. Furseĭ, Zh. Tekh. Fiz. **59**(5), 60 (1989) [Sov. Phys. Tech. Phys. **34**, 534 (1989)].
[7] A. V. Bushman, S. L. Leshkevich, G. A. Mesyats *et al.*, Dokl. Akad. Nauk SSSR **312**, 1368 (1990) [Sov. Phys. Dokl. **35**, 561 (1990)].
[8] G. N. Furseĭ, A. A. Antonov, and B. G. Gulin, Vest. Lenin. Univer., No. 10, 71 (1971).
[9] A. P. Komar, V. P. Savchenko, and V. N. Shrednik, Dokl. Akad. Nauk SSSR **129**, 540 (1959) [Sov. Phys. Dokl. **4**, 1286 (1959)].
[10] A. P. Komar and N. N. Syutkin, Dokl. Akad. Nauk SSSR **158**, 821 (1964) [Sov. Phys. Dokl. **9**, 872 (1965)].
[11] B. Jüttner and W. Rohrbeck, Preprint ZIE 76-3, Berlin, 1976.
[12] D. G. Myakishev, M. A. Tiunov, and V. P. Yakovlev, Int. J. Mod. Phys. A (Proc. Suppl.) 2B **2**, 915 (1993).
[13] G. P. Bazhenov, O. B. Ladyzhenskiĭ, E. A. Litvinov *et al.*, Zh. Tekh. Fiz. **47**, 2086 (1977) [Sov. Phys. Tech. Phys. **22**, 1212 (1977)].
[14] G. A. Mesyats and D. I. Proskurovskiĭ, *Pulsed Electric Discharges in Vacuum* [in Russian], Nauka, Novosibirsk, 1984.
[15] L. Tonks, Phys. Rev. **48**, 562 (1935).
[16] L. M. Baskin, Doctoral Dissertation in Physical-Mathematical Sciences [in Russian], Tomsk, 1990.
[17] A. V. Batrakov, S. A. Popov, and D. I. Proskurovskiĭ, Pis'ma Zh. Tekh. Fiz. **19**, 66 (1993) [Tech. Phys. Lett. **19**, 627 (1993)].

Translated by M. E. Alferieff

# ERRATA

## Erratum: QED corrections to DIS cross section with tagged photon [JETP Lett. 66, No. 6, 391–396 (25 September 1997)]

E. A. Kuraev
*Bogoliubov Laboratory of Theoretical Physics, JINR, 141980 Dubna, Russia*

N. P. Merenkov
*Kharkov Institute of Physics and Technology, 310108 Kharkov, Ukraine*
Pis'ma Zh. Eksp. Teor. Fiz. **67**, No. 4, 286 (25 February 1998)

[S0021-3640(98)01204-3]

PACS numbers: 13.60.Hb, 12.20.Ds, 99.10.+g

The list of authors for the article by E. A. Kuraev and N. P. Merenkov in JETP Lett. **66**, No. 6, pp. 391–396 (25 September 1997) should have been as follows:

H. Anlauf

*Fachbereich Physik, Siegen University, 57068 Siegen, Germany*

A. B. Arbuzov and E. A. Kuraev

*Bogoliubov Laboratory of Theoretical Physics, JINR, 141980 Dubna, Russia*

N. P. Merenkov

*Kharkov Institute of Physics and Technology, 310108 Kharkov, Ukraine*

The authors apologize for this oversight.

 © 1998 American Institute of Physics